Spring 2012

Simulations of the DARPA Suboff submarine including self-propulsion with the E1619 propeller

Nathan Chase
University of Iowa

SIMULATIONS OF THE DARPA SUBOFF SUBMARINE INCLUDING SELF-PROPULSION WITH THE E1619 PROPELLER

by

Nathan Chase

A thesis submitted in partial fulfillment
of the requirements for the Master of
Science degree in Mechanical Engineering
in the Graduate College
of The University of Iowa

May 2012

Thesis Supervisor: Associate Professor Pablo M. Carrica

Graduate College
The University of Iowa
Iowa City, Iowa

CERTIFICATE OF APPROVAL

_____

MASTER'S THESIS

_____

This is to certify that the Master's thesis of

Nathan Chase

has been approved by the Examining Committee
for the thesis requirement for the Master of Science
degree in Mechanical Engineering at the May 2012 graduation.

Thesis Committee: _____

Pablo M. Carrica, Thesis Supervisor

_____

Ching-Long Lin

_____

Frederick Stern

ACKNOWLEDGEMENTS

I would like to thank my advisor, Dr. Pablo Carrica. His guidance and encouragement throughout my graduate career has been instrumental. I would also like to thank my other committee members, Dr. Fred Stern and Dr. Ching-Long Lin, for taking time out of their schedules to assist me in this process.

I would like to also acknowledge the help I have received from other students at IIHR-Hydroscience and Engineering and the financial support from the Office of Naval Research under Grant N000141110232, with Dr. Ki-Han Kim as the program manager.

ABSTRACT

Simulations of the DARPA Suboff submarine and the submarine propeller E1619 using the overset flow solver CFDShip-Iowa V4.5 are presented. The hull was tested in a straight ahead simulation and also in a starboard turn. Propeller open water curves were obtained for two grids for a wide range of advance coefficients covering high to moderately low loads, and results compared with available experimental data. A verification study was performed for one advance coefficient ($J = 0.71$) on four grids and three time step sizes. The effect of the turbulence model on the wake was evaluated at $J = 0.4$ comparing results with RANS, DES, DDES, and with no turbulence model showing that RANS overly dissipates the wake and that in the solution with no turbulence model the tip vortices quickly become unphysically unstable. Tip vortex pairing is observed and described for $J \leq 0.71$ revealing multiple vortices merging for higher loads. The wake velocities are compared against experimental data for $J = 0.74$ showing good agreement. Self-propulsion computations of the DARPA Suboff generic submarine hull fitted with sail, rudders, stern planes, and the E1619 propeller were performed in model scale and the resulting propeller performance analyzed.

TABLE OF CONTENTS

LIST OF TABLES v

LIST OF FIGURES vi

CHAPTER

1 INTRODUCTION 1

1.1. Background 1
1.2. Objectives and Approach 4

2 COMPUTATIONAL METHODS 6

2.1. Overview 6
2.2. Mathematical Modeling 6
2.2.1. Governing Equations 6
2.2.2. Turbulence Modeling 7
2.2.3. Numerical Methods and Motion Controller 8

3 DARPA SUBOFF SUBMARINE 10

3.1. Straight-ahead Simulation 10
3.2. Turning Simulation 17

4 INSEAN E1619 PROPELLER 22

4.1. Geometry and Simulation Conditions 22
4.2. Verification and Validation 26
4.3. Open Water Curve 28
4.4. Wake Analysis 30
4.4.1. Grid Comparison 30
4.4.2. Wake Grid 31

5 SELF-PROPULSION 38

5.1. Simulation Conditions 38
5.2. Self-propelled Analysis 40
5.3. Blade Analysis 43

6 CONCLUSIONS AND RECOMMENDATIONS FOR FUTURE WORK 46

6.1. Conclusions 46
6.2. Recommendations for Future Work 47

REFERENCES 48

LIST OF TABLES

Table 3.1: DARPA Suboff and David Taylor Research Center Anechoic Flow Facility main parameters 10

Table 3.2: Grid dimensions for AFF-8 submarine 11

Table 3.3: DARPA Suboff fully-appended turning case main parameters 17

Table 3.4: Grid dimensions for AFF-8 submarine turning case 18

Table 4.1: INSEAN E1619 main propeller parameters 22

Table 4.2: Dimensions for grids used for verification study 24

Table 4.3: Details of the wake grid 25

Table 4.4: Numerical uncertainty from grid and time step convergence for $J = 0.71$ 28

Table 4.5: Different solver methods at $J = 0.4$ 34

Table 5.1: DARPA Suboff self-propelled by INSEAN E1619 main parameters 38

Table 5.2: Grid dimensions for self-propelled grid 39

Table 5.3: Self-propelled solution at $U = 2.75$ m/s 41

LIST OF FIGURES

Figure 3.1: AFF-8 and deep water towing tank grid 10
Figure 3.2: Resistance of Suboff Model 5470 12
Figure 3.3: AFF-8 wake at $x/L = 0.978$ 13
Figure 3.4: AFF-8 circumferentially averaged velocity at $x/L = 0.978$ 14
Figure 3.5: AFF-8 shear stress at $x/L = 0.978$ 14
Figure 3.6: AFF-8 wake at $x/L = 1.04$ 15
Figure 3.7: AFF-8 wake at $x/L = 1.2$ 15
Figure 3.8: View of the DARPA Suboff submarine in straight-ahead case 16
Figure 3.9: Rotating arm submarine turning case 17
Figure 3.10: View of the DARPA Suboff submarine in rotating arm turn 19
Figure 3.11: Turn velocity at $x/L = 0.978$ 19
Figure 3.12: Turn velocity vectors and vorticity at $x/L = 0.63$ 20
Figure 3.13: Turn velocity vectors and vorticity at $x/L = 0.84$ 21
Figure 4.1: Coarse grid system 22
Figure 4.2: Wake grid system 25
Figure 4.3: Convergence history of the thrust coefficient for different grids 26
Figure 4.4: Convergence history of the torque coefficient for different grids 27
Figure 4.5: Grid and time step convergence 27
Figure 4.6: E1619 OWC for wake and fine grids 29
Figure 4.7: $Q = 12{,}000$ isosurfaces at $J = 0.71$ for grids using DDES 30
Figure 4.8: Vorticity for all grids at $J = 0.71$ using DDES 31
Figure 4.9: $Q = 100{,}000$ isosurfaces for different turbulence models at $J = 0.4$ 32
Figure 4.10: Vorticity for different turbulence models at $J = 0.4$ 33
Figure 4.11: Q isosurfaces for all J's using DDES with the wake grid 34
Figure 4.12: Vorticity at different J's using DDES with the wake grid 35

Figure 4.13: Propeller velocity for $J = 0.74$ at $x = 0.17\ R$ (data from Liefvendahl *et al.* 2010).....36

Figure 5.1: Grid for self-propelled submarine computations.....38

Figure 5.2: Convergence history of boat velocity and propeller rotational speed...40

Figure 5.3: Cross sections of the wake at two axial positions (left) and at $y = 0$ (right) for self-propelled submarine.....42

Figure 5.4: View of the self-propelled DARPA Suboff submarine with vortical structures as isosurfaces of $Q = 10000$ 42

Figure 5.5: Thrust coefficient of three contiguous blades for three full rotations of the propeller. Blade 1 is on top at 0 degrees, with blade 2 the next one to port and blade 7 the previous to starboard.....43

Figure 5.6: Instantaneous wake at an axial location $R/2$ upstream of the propeller. Every 11^{th} vector is shown for clarity 45

CHAPTER 1

INTRODUCTION

1.1 Background

Propeller performance and efficiency are important parameters for all marine vehicles, but especially so on a submarine. A submarine propeller is optimized for noise reduction and therefore has more blades and is relatively larger than a ship propeller (Felli *et al*. 2008). Computational Fluid Dynamics (CFD) provides a more cost effective method of testing new propeller designs compared to Experimental Fluid Dynamics (EFD) as experimental prototypes are expensive and time consuming to create. CFD also enables more efficient optimization of propeller design due to shorter design cycles. Designers can quickly test different blade shapes, sizes, and number of blades without the cost of unnecessary fabrication. However, numerical simulations must be validated before extensive use on design and test purposes and CFD is costly compared to other simulation approaches, like potential flow methods.

Propeller forces have been studied and experimentally tested for over 70 years. Denny (1968) describes the process of obtaining propeller open water performance as it was done in the past. Current experimental procedures and corresponding uncertainty analysis are periodically updated by the International Towing Tank Conference (2002). Though submarine data is mostly unavailable, experimental results for the generic submarine propeller INSEAN E1619 were reported by Di Felice *et al.* (2009), who studied open water performance and the wake of the propeller under various loads. Pitot tubes, hot-wire, Laser Doppler Velocimetry (LDV) and Particle Image Velocimetry (PIV) techniques have all been used to measure the wake of propellers. Inoue and Kuroumaru (1984) first investigated the structure and decay of vorticity of an impeller flow field utilizing a slanted single hot-wire. As technology advanced, LDV and PIV have become the preferred methods for wake analysis as they allow more efficient data acquisition and easy reconstruction of a flow field cross section (Di Felice *et al*. 2009, Felli *et al*. 2011).

The most common numerical methodologies for studying propeller flows are classified as potential flow or CFD approaches although other methods such as actuator disc can be used. Potential flow models are cheaper and easier to use, however they are reliable only if minor viscous effects are expected. The relative simplicity of potential flow codes enabled them to be used when computers were still in their infancy, and thus have been used longer than CFD codes. CFD is more accurate and can capture the wake and highly transient effects, but it is considerably more expensive.

A potential flow low-order 3-D boundary element method was used by Young and Kinnas (2003) to evaluate supercavitating and surface-piercing propellers. The simulation's predicted results compare well with experimental measurements for steady inflow. Fuhs (2005) evaluated PUF-2, PUF-14, MPUF-3A, and PROPCAV solvers with DTMB propellers 4119, 4661, 4990, and 5168 under different conditions. He found that none of these potential flow solvers performed significantly better than the others under non-cavitating conditions.

Gatchell *et al.* (2011) evaluated open water propeller performance using the potential flow panel code PPB and the Reynolds averaged Navier-Stokes (RANS) solver FreSCo+. The codes gave similar results at advance coefficient (J) values higher than 1.3 but PPB dramatically under predicted the torque and thrust at lower J's. Watanabe *et al.* (2003) showed that the RANS solver Fluent version 6.1 predicted thrust and torque coefficients in agreement with the measurements taken from uniform flow. Califano and Steen (2011) found that a RANS simulation on a generic propeller provides satisfactory values when compared to experimental results at low J's but became inaccurate at higher J's. They concluded that the inability of the RANS model to resolve tip vortices was the cause of the discrepancies. Hsiao and Pauley (1999) attempted to reduce the inaccuracies of a RANS model by incorporating the Baldwin-Barth turbulence method with RANS computations to compute tip vortex flows around the P5168 propeller. The general flow characteristics were in agreement with the measured values but the tip vortex was overly

diffused. Rhee and Joshi (2005) also simulated the P5168 propeller utilizing a k-w turbulence model and found that the thrust and torque values are in good agreement with measured values, but turbulence quantities in the tip vortex region were under-predicted.

To resolve the unsteady flow field behind a DTMB 4118 propeller, Yu-cun and Huai-xin (2010) employed Detached-Eddy Simulation (DES) modeling. DES resolves the tip vortices better than RANS because the turbulent viscosity is reduced where the grid is fine enough to capture large vortices. The DES calculated open water curve (OWC) and experimental OWC showed great similarity with the trends being virtually identical. Yu-cun and Huai-xin (2010) were also able to calculate vortex structures in the flow and accurately predict the pressure distribution at different blade sections. Castro *et al.* (2011) simulated the KP 505 propeller using DES to obtain the OWC and determine the self-propulsion point for the KRISO container ship KCS. In that case, the OWC was measured at model-scale but was simulated at full-scale. Despite the differences in propeller size, the OWCs indicated very good agreement between the simulated and experimental results.

CFD self-propulsion simulations usually utilize a body force model of the propeller rather than the direct modeling method used by Carrica *et al*. (2010, 2011). Direct modeling is less commonly used because the propeller rotates much faster than the ship advances, necessitating a small time step to provide sufficient resolution of the propeller flow. While a body force model provides acceptable results for hull analysis, a discretized propeller is needed to fully investigate the interaction of wake and appendages with the propeller. Liefvendahl *et al.* (2010) and Liefvendahl and Tröeng (2011) used a Large Eddy Simulation (LES) method to simulate the E1619 propeller wake in both free stream and under moving conditions using the Defense Advanced Research Projects Agency (DARPA) Suboff submarine hull near self-propulsion, reporting OWC results as well as transient loads on the propeller and individual blades. A discretized propeller was

also used by Carrica *et al.* (2010) for a self-propelled ship, and this technique is applied in this paper to the DARPA Suboff submarine propelled by the E1619 propeller.

The flow around the DARPA Suboff has previously been computed without a propeller by Bull (1996) and by Rhee (2003). Alin *et al.* (2010) computed the flow around the Suboff body both with and without an actuator disk propeller model. Vaz *et al.* (2010) computed the Suboff body in both straight-ahead conditions and at an angle of incidence.

1.2 Objectives and Approach

This work utilized the code CFDShip-Iowa V4.5 (Carrica *et al*. 2007a, 2007b) to study the DARPA Suboff submarine and the generic propeller E1619. The performance of different turbulence modeling approaches to obtain the OWC and the vortical structure of the generic submarine propeller INSEAN E1619 were evaluated. RANS, DES, Delayed Detached-Eddy Simulation (DDES), and with No Turbulence Model (NTM) simulations were performed at a single advance coefficient ($J = 0.4$). The OWC and the vortical structure were found using DDES at six different J's.

A validation and verification study with four different grids and three time steps was performed for one advance coefficient ($J = 0.71$) using experimental data from INSEAN. Uncertainty analysis was performed utilizing the procedures described in (Stern et al. 2001a, 2001b) to estimate the grid, time step, and total errors. The wake profile was further analyzed utilizing a grid with an extra refinement block behind the propeller. Vorticity and isosurface results from this wake grid were compared to the fine grid results, and tip vortex resolution and vortex pairing were evaluated. The propeller was then attached to the DARPA Suboff geometry and the self-propulsion point was found, along with the propeller performance at the aforementioned point. Computations of the captive DARPA Suboff were performed under several conditions to test the ability of the code to simulate this type of geometry.

The Suboff model was chosen due to the large amount of experimental data available. Experimental information on submarine hulls is largely unobtainable since most countries prefer not to share that information. Suboff has publicly available data for hull resistance in addition to velocity and pressure fields for straight ahead and rotating arm experiments.

CHAPTER 2

COMPUTATIONAL METHODS

2.1 Overview

The simulations were performed with CFDShip-Iowa v4.5 (Carrica *et al*. 2007a, 2007b), a CFD code with RANS, DES, and DDES capabilities. It uses dynamic overset grids to resolve large-amplitude motions and a single-phase level set approach to model the free surface. The RANS and DES approaches are based on a blended $k-\omega/k-\epsilon$ shear stress transport (SST) turbulence model (Menter 1994). Rigid-body motion computations with six degrees of freedom are possible and can incorporate moving control surfaces and modeled or resolved propulsors. CFDShip-Iowa is capable of including regular and irregular waves, maneuvering controllers, and autopilot and has been validated for steady-state and dynamic problems (Carrica *et al*. 2007a, 2007b).

2.2 Mathematical Modeling

2.2.1 Governing Equations

The incompressible Navier-Stokes equations are non-dimensionalized using the reference velocity U_0 and a characteristic length L. The mass and momentum conservation equations are written as:

$$\frac{\partial u_j}{\partial x_j} = 0 \tag{1}$$

$$\frac{\partial u_i}{\partial t} + \frac{\partial u_i u_j}{\partial x_j} = -\frac{\partial p}{\partial x_i} + \frac{\partial}{\partial x_j}\left[\frac{1}{Re_{eff}}\left(\frac{\partial u_i}{\partial x_j} + \frac{\partial u_j}{\partial x_i}\right)\right] + s_i \tag{2}$$

where the dimensionless piezometric pressure is $p = p_{abs}/\rho U_0^2 + 2k/3$ and p_{abs} is the absolute pressure. The effective Reynolds number is $1/Re_{eff} = 1/Re + v_t$, with the turbulent viscosity v_t obtained from the turbulence model.

2.2.2 Turbulence Modeling

The turbulence model used is a blended $k-\omega/k-\epsilon$ model. The turbulent kinetic energy k and the specific dissipation rate ω are computed from the transport equations for the $k-\omega$ model:

$$\frac{\partial k}{\partial t}+\left(u_j-\sigma_k\frac{\partial v_t}{\partial x_j}\right)\frac{\partial k}{\partial x_j}-\frac{1}{P_k}\frac{\partial^2 k}{\partial x_j^2}+s_k=0 \tag{3}$$

$$\frac{\partial \omega}{\partial t}+\left(u_j-\sigma_\omega\frac{\partial v_t}{\partial x_j}\right)\frac{\partial \omega}{\partial x_j}-\frac{1}{P_\omega}\frac{\partial^2 \omega}{\partial x_j^2}+s_\omega=0 \tag{4}$$

The turbulent viscosity is $v_t=k/\omega$ and the Peclet numbers are defined as:

$$P_k=\frac{1}{1/Re+\sigma_k v_t}, \qquad P_\omega=\frac{1}{1/Re+\sigma_\omega v_t} \tag{5}$$

The source for k and ω are

$$s_k=-G+\beta^*\omega k \tag{6}$$

$$s_\omega=\omega\left(\beta^*\omega-\gamma\frac{G}{k}\right)-2(1-F_1)\sigma_{w2}\left(\frac{\partial k}{\partial x_j}\right)\left(\frac{\partial \omega}{\partial x_j}\right)\frac{1}{\omega} \tag{7}$$

where

$$G=v_t\tau:\left(\frac{\partial u}{\partial x_j}\right) \tag{8}$$

$$F_1=\tanh\left[\left(\min\left(\max\left(\frac{\sqrt{k}}{0.09\omega\delta};\frac{1}{Re}\frac{500}{\delta^2\omega}\right);\frac{4\sigma_{\omega 2}k}{CD_{kw}\delta^2}\right)\right)^4\right] \tag{9}$$

$$CD_{k\omega}=\max\left(2\sigma_{\omega 2}\frac{1}{\omega}\left(\frac{\partial k}{\partial x_j}\right)\left(\frac{\partial \omega}{\partial x_j}\right);10^{-20}\right) \tag{10}$$

The blending function F_1 switches from zero in the wake region to one in the logarithmic and sublayer regions of boundary layers. In order to calculate F_1 the distance to the nearest no-slip surface, δ, is needed.

The SST model is a user specified option that accounts for turbulent stresses transport. This inclusion improves the results for flows containing opposing pressure gradients. The model varies from the blended $k-\omega/k-\epsilon$ model with the absolute value of the vorticity, Ω, used to define the turbulent viscosity as:

$$v_t = \frac{0.31k}{\max(0.31\omega;\Omega F_2)} \tag{11}$$

$$F_2 = \tanh\left[\left(\max\left(\frac{2\sqrt{k}}{0.09\omega\delta};\frac{500v}{\delta^2\omega}\right)\right)^2\right] \tag{12}$$

2.2.3 Numerical Methods and Motion Controller

The regions of massively separated flows can be modeled using $k-\omega/k-\epsilon$ based DES or DDES models. The dissipative term of the *k*-transport equation is revised as:

$$D_{RANS}^k = \rho\beta^* k\omega = \frac{\rho k^{3/2}}{l_{k-w}} \tag{13}$$

$$D_{DES}^k = \rho\frac{k^{3/2}}{\tilde{l}} \tag{14}$$

The length scales are:

$$l_{k-\omega} = k^{1/2}/(\beta^*\omega) \tag{15}$$

$$\tilde{l} = min(l_{k-\omega}, C_{DES}\Delta) \tag{16}$$

where $C_{DES} = 0.65$ and Δ is the local grid spacing. This formulation determines where the LES or RANS models will be applied. A detailed description of the DES and DDES implementation into CFDShip-Iowa is found in (Xing *et al*. 2007) and (Xing *et al*. 2010), respectively.

The self-propelled simulation used a proportional-integral speed controller to alter the propeller RPS to achieve the target speed. The instantaneous RPS is computed as

$$n = Pe_U + I\int_0^t e_U dt \tag{17}$$

where P and I are the proportional and integral constants of the control and the velocity error is defined as $e_U = U_{boat} - U_{target}$.

CHAPTER 3

DARPA SUBOFF SUBMARINE

3.1 Straight-ahead Simulation

Table 3.1: DARPA Suboff and David Taylor Research Center Anechoic Flow Facility main parameters

Reynolds number	1.2×10^7
	DARPA Suboff
Hull Diameter [m]	0.508
Hull Length [m]	4.356
	DTRC AFF
Wind Tunnel Width [m]	2.44
Wind Tunnel Height [m]	2.44
Wind Tunnel Length [m]	4.19

Velocity fields for the fully-appended DARPA Suboff were experimentally studied at the David Taylor Research Center Anechoic Flow Facility (Groves *et al.* 1989) under the conditions listed in Table 3.1.

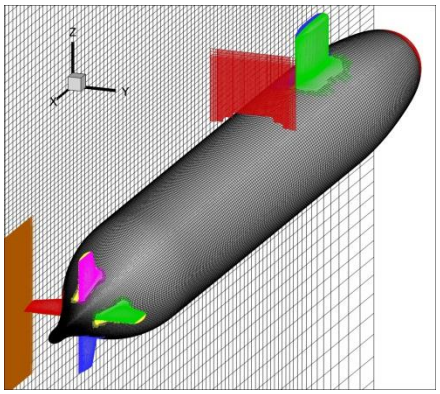

Figure 3.1: AFF-8 and deep water towing tank grid.

All grids, shown in Fig. 3.1, were constructed to satisfy the $y^+ = 1$ requirement of the $k - \omega/k - \epsilon$ turbulence model with near-wall integration. The boat grid, listed in

Table 3.2, consists of a hull grid ('O' type) and overlapping appendage grids intended to provide a fine computational mesh for the wake. A Cartesian background grid is used to impose wind tunnel boundaries, and two Cartesian refinement grids are used, one to better capture the sail wake and the other grid to capture the wake of the boat. The domain connectivity needed to perform overset computations was obtained using the code Suggar (Noack, 2005) while surface overlap was pre-processed using Usurp (Boger and Dreyer, 2006) to integrate the forces.

Table 3.2: Grid dimensions for AFF-8 submarine

Grid	Size	Total Points	Type
Hull	361x61x151	3.33 M	'O'
Nose	61x51x61	190 k	Wrapped
Sail	2x61x51x121	2x376 k	Wrapped
Rudders	4x61x51x61	4x190 k	Wrapped
Stern Planes	4x61x51x61	4x190 k	Wrapped
Refinement 1	351x109x101	3.86 M	Cartesian
Refinement 2	277x205x205	11.6 M	Cartesian
Background	187x109x109	2.22 M	Cartesian
Total		23.5 M	

A fourth-order biased scheme was used for convection for the momentum equations with a second-order centered scheme used for diffusion and a second-order backward discretization used in time. The turbulence equations used the same schemes for diffusion and time but differed from the momentum equations by utilizing a second-order upwind scheme for convection. The boundary conditions used were: no-slip for the hull and appendages, imposed incoming velocity for the inlet, zero normal second derivative for the exit, and farfield conditions for the tank.

Before computing self-propulsion a set of computations were performed for DARPA Suboff towed in fully appended configuration without a propeller. These results

were compared against the data by Crook (1990), who measured the resistance in a deep water towing tank. Figure 3.2 shows that the resistance predicted by RANS and DDES computations is very close to the experimental values, and that DDES shows accurate predictions for a wide range of speeds.

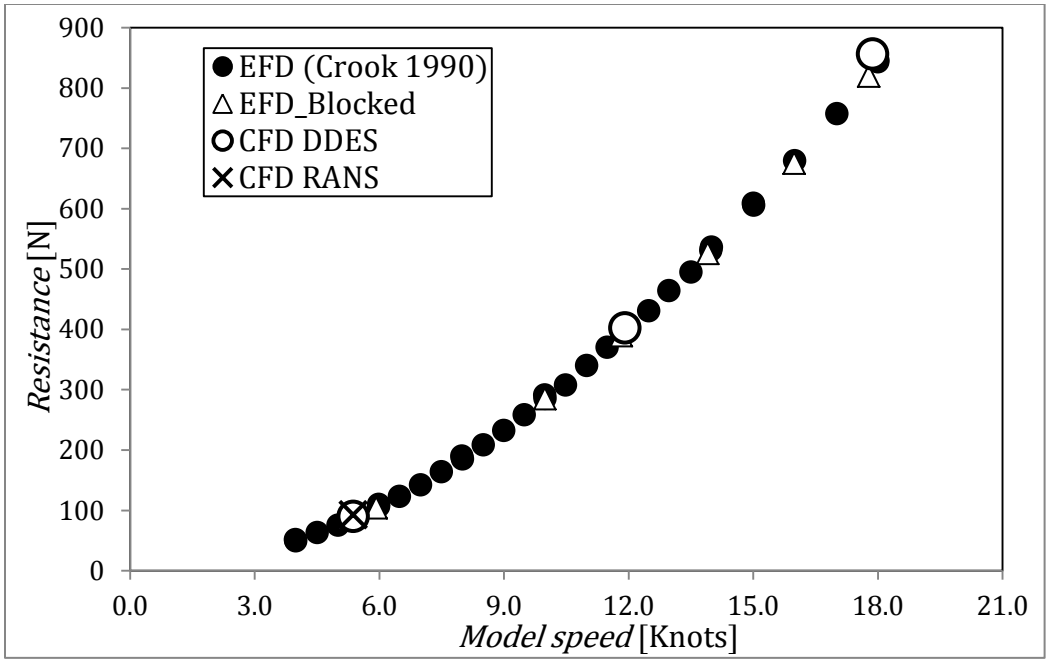

Figure 3.2: Resistance of Suboff Model 5470.

RANS and DDES were used to simulate the submarine moving straight ahead. The wake was analyzed at the location $x/L = 0.978$ for both simulations and the experimental cases and shown in Fig 3.3. The hole in the center of each wake profile is due to the trailing edge of the submarine and this testing void was duplicated for all locations. The overall pattern of each wake is very similar, with reduced flow velocity downstream of the appendages. Notice the high velocity observed in the wake of the sail, where necklace vortices deplete the boundary layer at the center and send low-momentum flow to the sides, causing a "V" shaped high-speed carving in the wake.

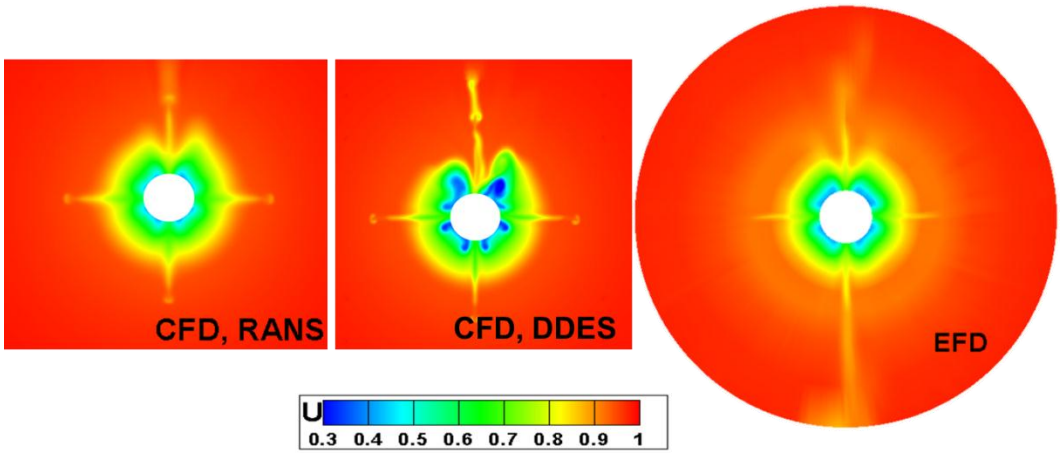

Figure 3.3: AFF-8 wake at $x/L = 0.978$.

The circumferentially averaged velocity is shown in Fig. 3.4 for RANS, DDES, and EFD. The average velocity was found by creating a 360 node circular grid, one degree separation between each node, and interpolating the RANS solution at each of those locations. This procedure was repeated all radii and also for DDES and EFD solutions. The two numerical simulations predicted almost the same value at large radii (larger than $R = 0.72$) but are a higher velocity than EFD. The largest difference occurs at $R = 0.92$ where the RANS velocity is 3.85% higher than experimental and the DDES velocity is 3.95% higher. RANS begins to underpredict the velocity near the hull, ultimately yielding a -12.9% error at $R = 0.25$ compared to the 2.13% experienced by DDES at that same radius.

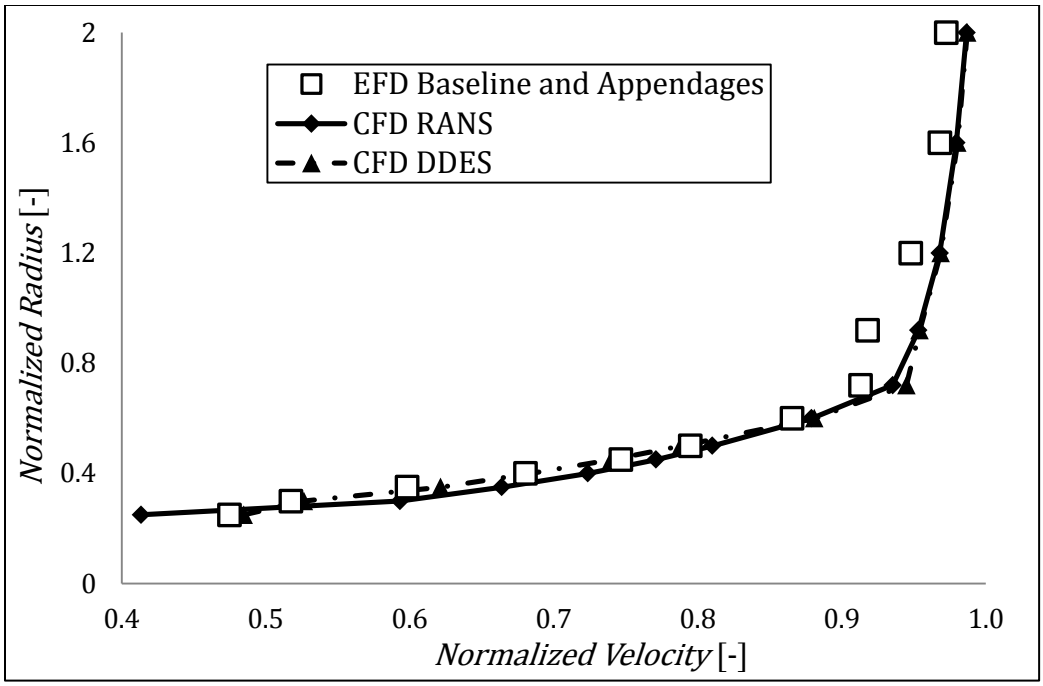

Figure 3.4: AFF-8 circumferentially averaged velocity at $x/L = 0.978$.

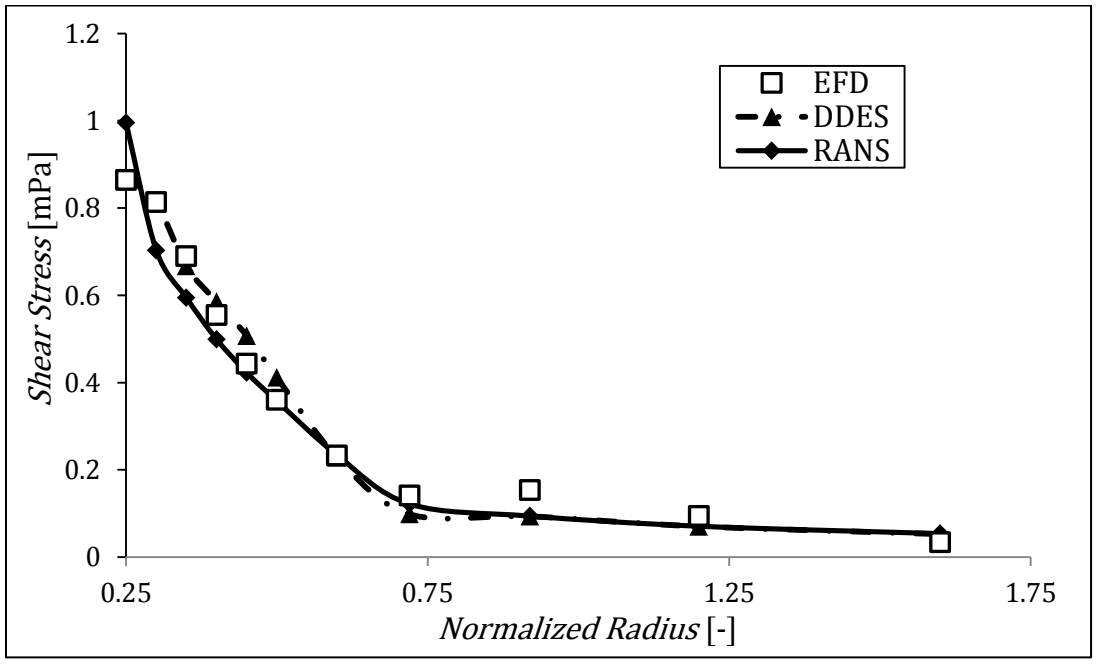

Figure 3.5: AFF-8 shear stress at $x/L = 0.978$.

The shear stress is shown in Fig. 3.5 for RANS, DDES, and EFD. With the exception of the first and last radius, the stress predicted by RANS is always lower than the measured experimental value. DDES predictions are closer to experimental than RANS with most of the data points being within 5% of the measured values.

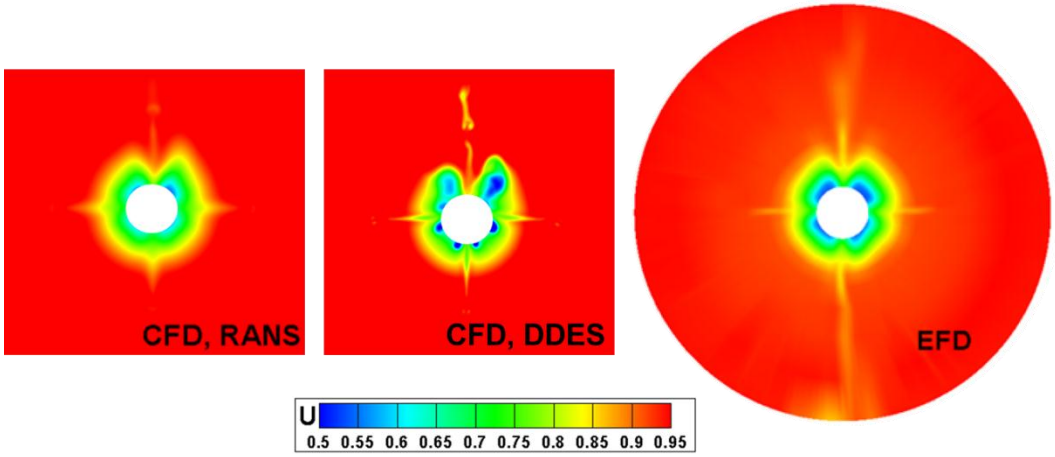

Figure 3.6: AFF-8 wake at $x/L = 1.04$.

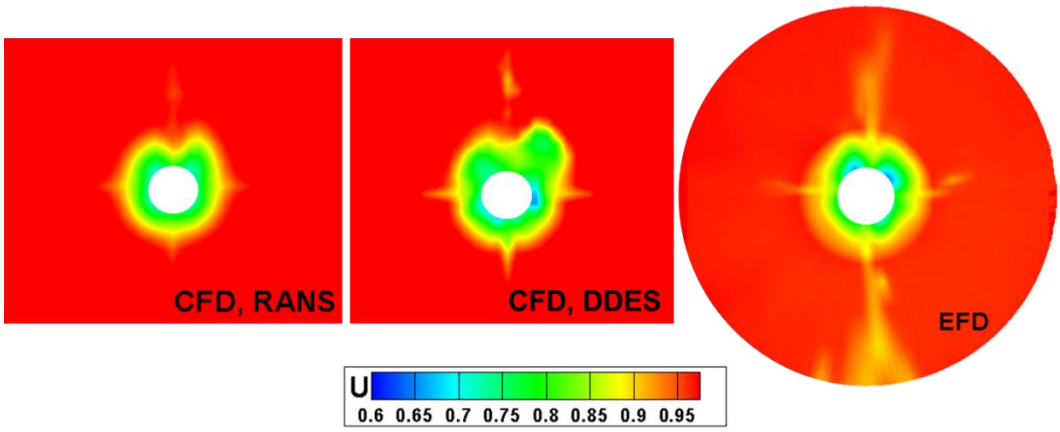

Figure 3.7: AFF-8 wake at $x/L = 1.2$.

The wake profile was similarly evaluated downstream as previously done for $x/L = 0.978$. Figure 3.6 and 3.7 show the wake at $x/L = 1.04$ and $x/L = 1.2$. The wake pattern is in good agreement with experiments. As expected, RANS predicts a more

diffused wake, while DDES tends to overpredict the effects of the sail on the flow field causing a sharp contrast between the high speed flow immediately trailing the sail and the low speed necklace wake. The wake shows a predictable trend as the flow becomes more uniform farther away from the boundary layer effects of the submarine.

Figure 3.8 shows the submarine as it travels straight-ahead in the CFD DDES simulation. The hull of the boat is colored by pressure while the slices are colored by axial velocity. The wake development details can be observed as the boundary layer gets thinner immediately downstream of the sail and thicker on the sides of this depleted area.

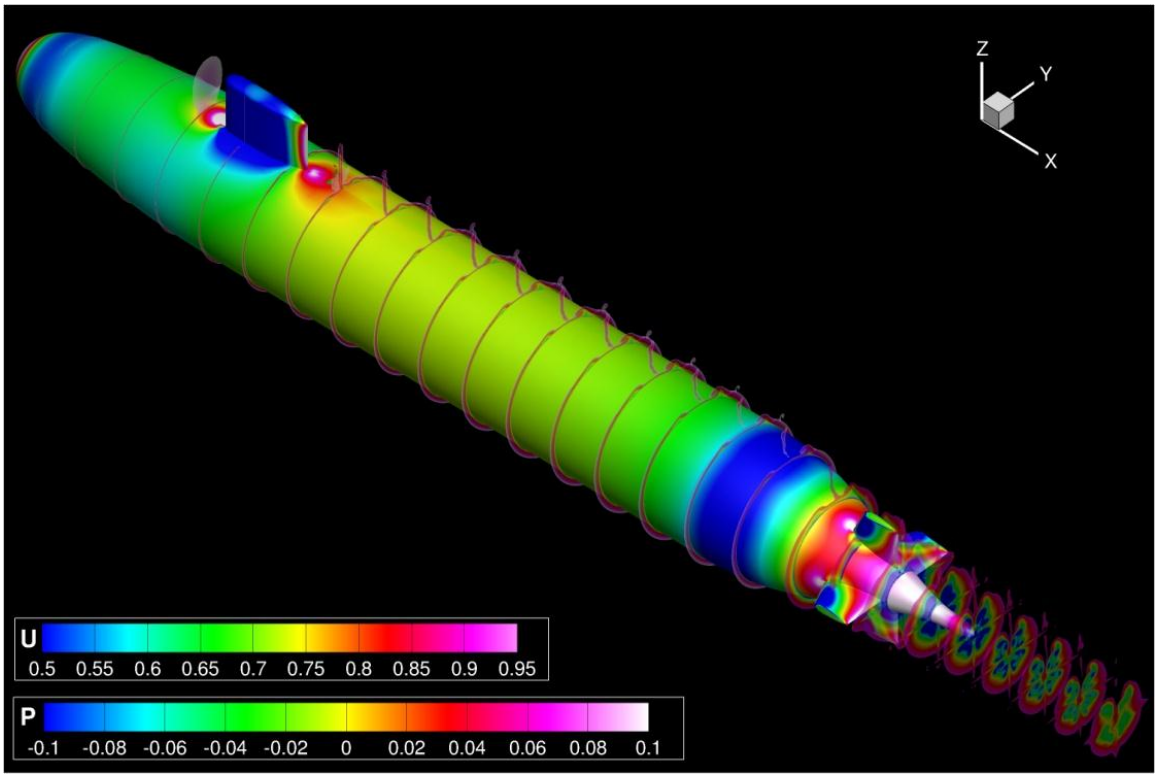

Figure 3.8: View of the DARPA Suboff submarine in straight-ahead case.

3.2 Turning Simulation

Table 3.3: DARPA Suboff fully-appended turning case main parameters.

Reynolds number	$6.53x10^6$
Velocity [knots]	3
Rudder Angle [^{o}]	- 10
β [^{o}]	8.2

The Suboff submarine was experimentally tested completing a starboard turn with a drift angle (β) ranging between 3.8^o and 16.5^o for the bare hull and a single test of $\beta = 8.2^o$ for the fully-appended model. The steady turning experiments were performed at Naval Surface Warfare Center Carderock Division in the Rotating Arm Basin. Static pressure along the hull surface was measured with twenty-three pressure taps at each location, $x/L = 0.63$ and $x/L = 0.84$. Stereo PIV was used at the same axial locations as the pressure measurements to capture the wake during the turn. The fully appended simulation shown in Fig 3.9 was initialized in the middle of the $\beta = 8.2^o$ turn, rotating for 90^o with a $\Delta t = 0.002$ and the parameters are listed in Table 3.3.

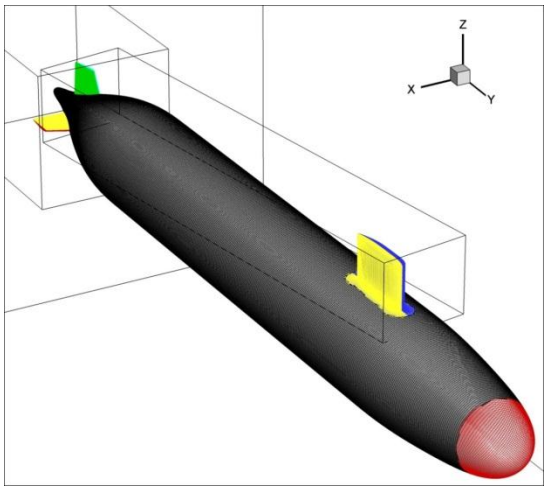

Figure 3.9: Rotating arm submarine turning case.

The turning case grids, found in Table 3.4, were constructed in the same manner as was described in the straight-ahead simulation with a few minor changes. The hull grid density was increased, as was the density on the rudders and stern planes. The density of the refinement grid trailing the sail was also increased and the grid direction reoriented, whereas the secondary refinement grid was coarsened for a total grid increase of 2.9 M nodes.

Table 3.4: Grid dimensions for AFF-8 submarine turning case.

Grid	Size	Total Points	Type
Hull	481x101x241	11.7 M	'O'
Nose	61x51x61	190 k	Wrapped
Sail	2x61x51x121	2x376 k	Wrapped
Rudders	4x61x51x121	4x376 k	Wrapped
Stern Planes	4x61x51x121	4x376 k	Wrapped
Propeller Hub	101x37x101	377 k	'O'
Refinement Gaps for Appendages	4x84x87x26	4x190 k	Curvilinear Block
Refinement Sail Wake	386x121x111	5.18 M	Cartesian
Refinement Wake	187x109x109	2.22 M	Cartesian
Background	187x109x109	2.22 M	Cartesian
Total		26.4 M	

Figure 3.10 shows the submarine as it travels in the CFD rotating arm simulation. The hull of the boat is colored by pressure while the slices are colored by total velocity to display the boundary layer. The vortical structures, also colored by total velocity, are shown as isosurfaces of $Q = 100$. It is noticeable the effect of the necklace vortex on the boundary layer, causing again a boundary layer depletion that the cross flow from the rotation transports to starboard. The sail tip vortex rolls the low velocity wake flow from the sail. The rudders produce significant tip vortices, indicating that under these conditions the incoming flow angle of attack is large. The necklace vortices from the rudders are very strong and become unstable, forming braided vortical wakes.

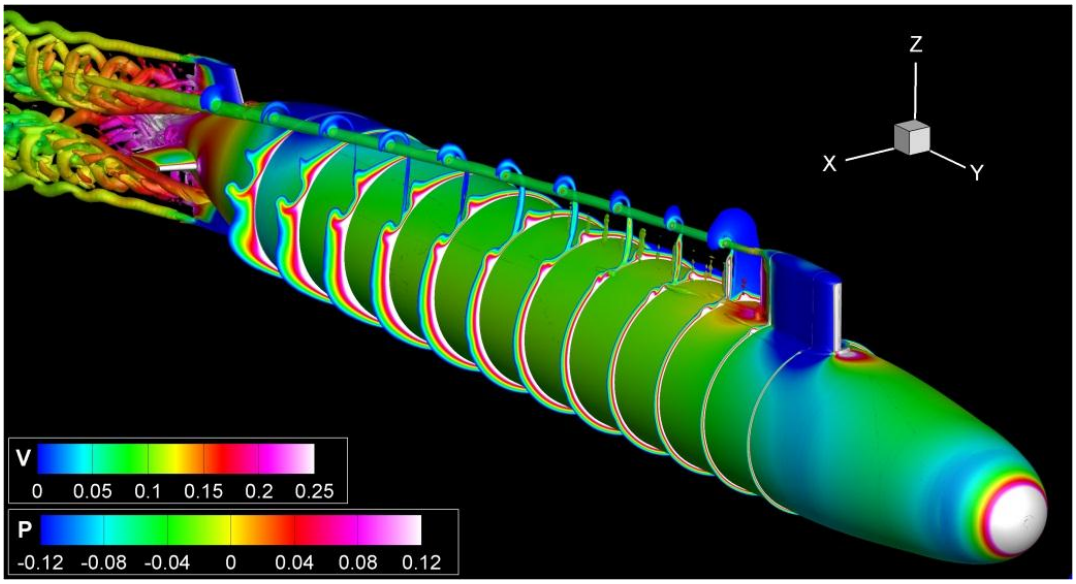

Figure 3.10: View of the DARPA Suboff submarine in rotating arm turn.

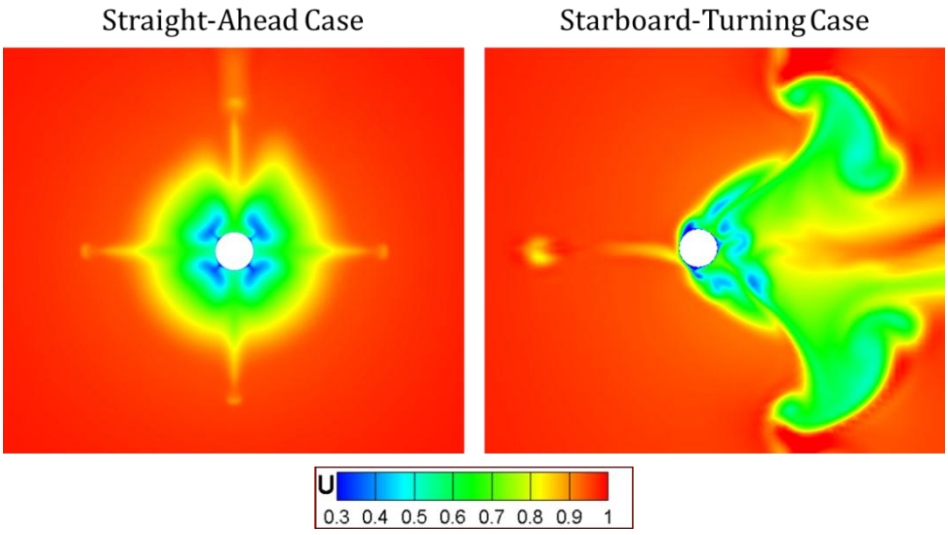

Figure 3.11: Turn velocity at $x/L = 0.978$.

The wake at $x/L = 0.978$ was compared to the straight-ahead case to analyze how the flow was change by the turning motion in Fig 3.11. The turning case exhibits an almost horizontally symmetrical flow field with small influences from the sail. A vortex

from the tip of the port side stern plane is noticeable, although there is only marginal flow impact from the rest of the stern plane. The effect of the other stern plane is lost among the strong wake created by the drifting hull. The drifting hull is also largely responsible for the large flow disturbance caused by the rudders, including the tip vortices seen at the top and bottom of the frame.

The vorticity found in the PIV experiment was compared to the CFD result at $x/L = 0.63$ in Fig 3.12. Color was omitted for vorticity values between -15 and 15 to match the format of the experimental results (Atsavapranee 2010). The experimental axis scales were also duplicated for proper comparison. There is good agreement between CFD and experiments for the magnitude and location of the vorticity caused by the hull. The sail tip vortex is also very well predicted, both in location and magnitude.

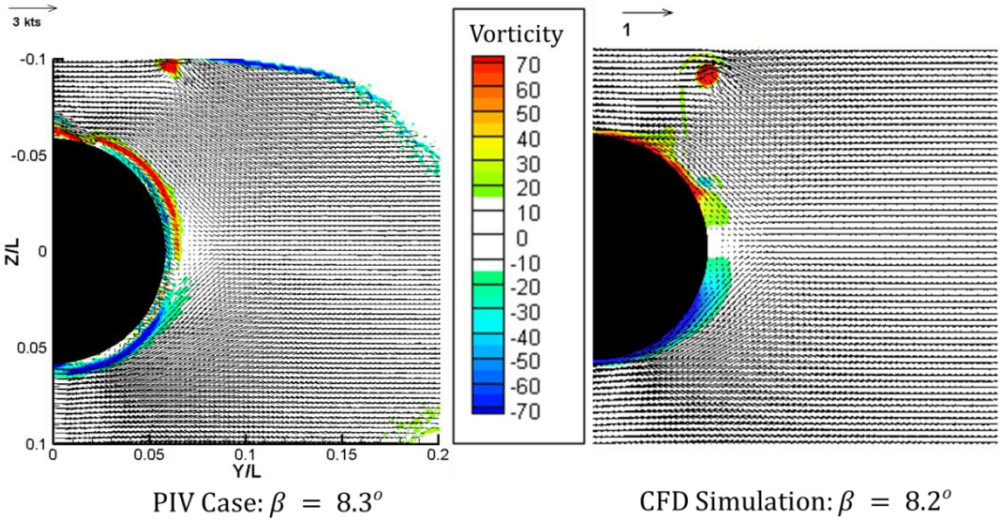

Figure 3.12: Turn velocity vectors and vorticity at $x/L = 0.63$.

Vorticity was also compared at $x/L = 0.84$, shown in Fig. 3.13, with CFD and PIV in good agreement even though the drift angle in the experiment is 9% larger. While the trends and magnitudes of vorticity are similar for both cases, CFD tends to diffuse the vortical structures as evidenced by the less concentrated intensity in the sail tip vortex.

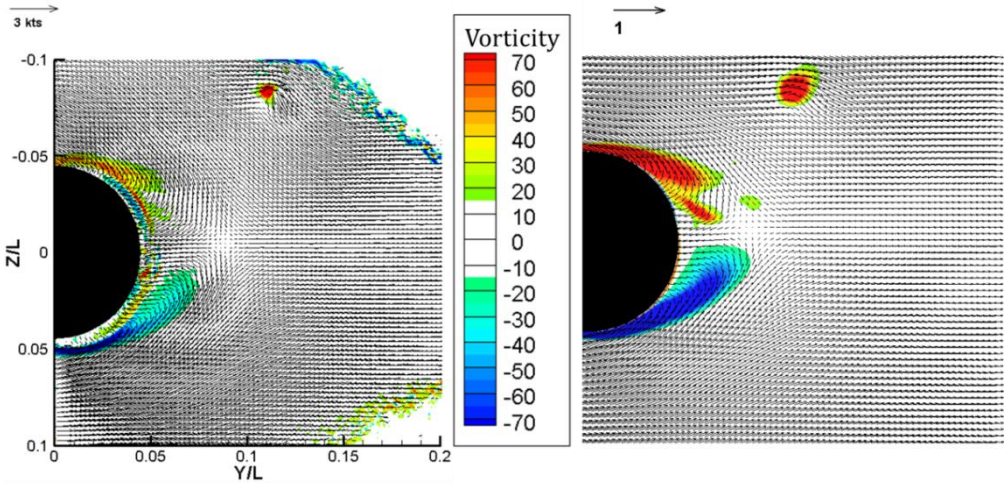

Figure 3.13: Turn velocity vectors and vorticity at $x/L = 0.84$.

CHAPTER 4

INSEAN E1619 PROPELLER

4.1. Geometry and Simulation Conditions

Table 4.1: INSEAN E1619 main propeller parameters

	INSEAN E1619
Number of blades	7
Diameter [mm]	485
Hub Diameter Ratio	0.226
Pitch at r = 0.7 R	1.15
Chord at 0.75 R [mm]	6.8

The geometry of interest is the E1619 propeller, a seven bladed design by INSEAN shown in Fig. 4.1. The propeller used in the experiments was created from one single piece of avional aluminum alloy with a black anodized outer skin (Di Felice *et al*. 2009). The propeller's main parameters are shown in Table 4.1. Open water experiments were performed in the INSEAN towing tank, and wake velocity measurements were made with LDV in a closed test loop.

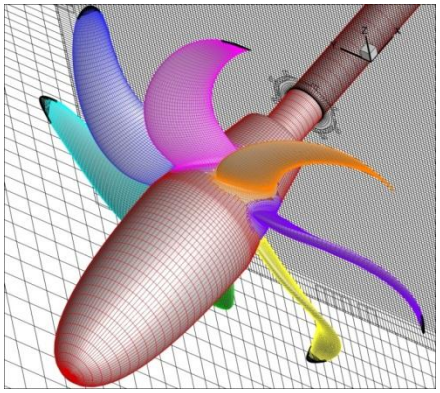

Figure 4.1: Coarse grid system.

The overset grid system, shown in Fig. 4.1, was designed to rotate as a rigid body in the Earth system of coordinates. All grids were constructed to satisfy the $y^+ = 1$

requirement of the $k-\omega/k-\epsilon$ turbulence model with near-wall integration. Each blade consists of a blade grid ('O' type) and a tip grid intended to close the blade and provide a fine computational mesh for the tip vortices. The blade grids overlap with an 'O' shaft grid that contains the hub and the shaft profile. A Cartesian background grid is used to impose the far-field, inlet and exit boundary conditions, and a Cartesian refinement grid is used to better capture the wake of the propeller. The code Suggar (Noack, 2005) was used to obtain the domain connectivity needed to perform overset computations. To integrate the forces the surface overlap was pre-processed using Usurp (Boger and Dreyer, 2006).

A grid for the shaft and hub alone was constructed by removing the blades from the grids in Table 4.2, and used to correct the propeller thrust and torque by subtracting the shaft/hub forces from the full grid forces, as done in the experiments. These corrections are very minor.

For the momentum equations and all runs a fourth-order biased scheme was used for convection, a second-order centered scheme was used for diffusion and a second-order backward discretization was used in time. The same was used for the turbulence equations but with a second-order upwind scheme for convection. No-slip boundary conditions were used for the shaft, hub and blades, imposed incoming velocity for the inlet, zero normal second derivative for the exit, and farfield conditions for the side of the domain.

Table 4.2: Dimensions for grids used for verification study

Grid	Size (Coarse, Medium, Fine, Very Fine)	Total Points (Coarse, Medium, Fine, Very Fine)	Type
Shaft	159x29x80 201x37x101 253x46x127 318x57x159	369 k 751 k 1.48 M 2.88 M	'O'
Blades (1-7)	7x80x29x80 7x101x37x101 7x127x46x127 7x159x57x159	7x186 k 7x377 k 7x742 k 7x1.44 M	'O'
Tips (1-7)	7x48x40x48 7x61x51x61 7x76x64x76 7x95x80x95	7x92.2 k 7x190 k 7x370 k 7x722 k	Wrapped
Refinement	191x175x175 241x221x221 303x278x278 381x350x350	5.85 M 11.8 M 23.4 M 46.7 M	Cartesian
Background	148x86x86 187x109x109 235x137x137 295x172x172	1.09 M 2.22 M 4.41 M 8.73 M	Cartesian
Total		9.26 M 18.7 M 37.1 M 73.4 M	

For the grid convergence study, four grids (coarse, medium, fine and very fine) were generated. A grid coarsening factor of $\sqrt{2}$ was applied in each direction with a trilinear interpolation algorithm to the very fine grid to obtain the fine grid so that each grid shape and point distribution would be as close to the source grid as possible. This procedure was then repeated to create the medium and coarse grids. Details of the grids are summarized in Table 4.2.

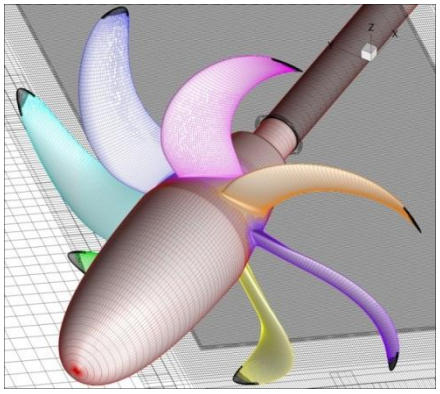

Figure 4.2: Wake grid system.

An additional grid was constructed to better capture the wake. The wake grid, shown in Fig. 4.2, was created by taking the medium grid and adding a very fine refinement block immediately downstream of the propeller blades. This block was added to calculate the wake and tip vortices with much better accuracy than it was possible with the previous grid system. The refinement grid added to the wake matches the grid size of the fine grids used for the tips of the blades, thus providing a grid of consistent refinement for the tip vortices in the wake. The wake grid is summarized in Table 4.3.

Table 4.3: Details of the wake grid

Grid	Size	Total Points	Type
Shaft	201x37x101	751 k	'O'
Blades (1-7)	7x101x37x101	7x377 k	'O'
Tips (1-7)	7x61x51x61	7x190 k	Wrapped
Refinement 1	361x386x386	53.8 M	Cartesian
Refinement 2	241x221x221	11.8 M	Cartesian
Background	187x109x109	2.22 M	Cartesian
Total		72.5 M	

4.2. Verification and Validation

A grid convergence study was performed at $J = 0.71$ using DDES. The convergence histories of the thrust coefficient K_T and torque coefficient K_Q for all grids are shown in Figs. 4.3 and 4.4, respectively. The time step, t_i/t_{max}, was nondimensionalized using the last calculated time step of each specific simulation. These figures show that the thrust and torque converge in time and that as the grid is refined both K_T and K_Q tend to converge to smaller values, with faster convergence for K_T.

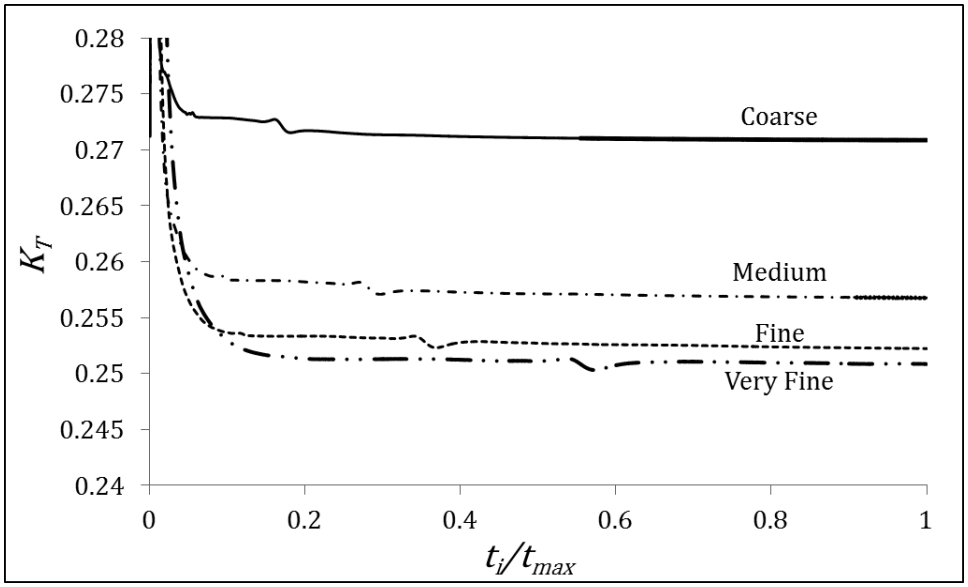

Figure 4.3: Convergence history of the thrust coefficient for different grids.

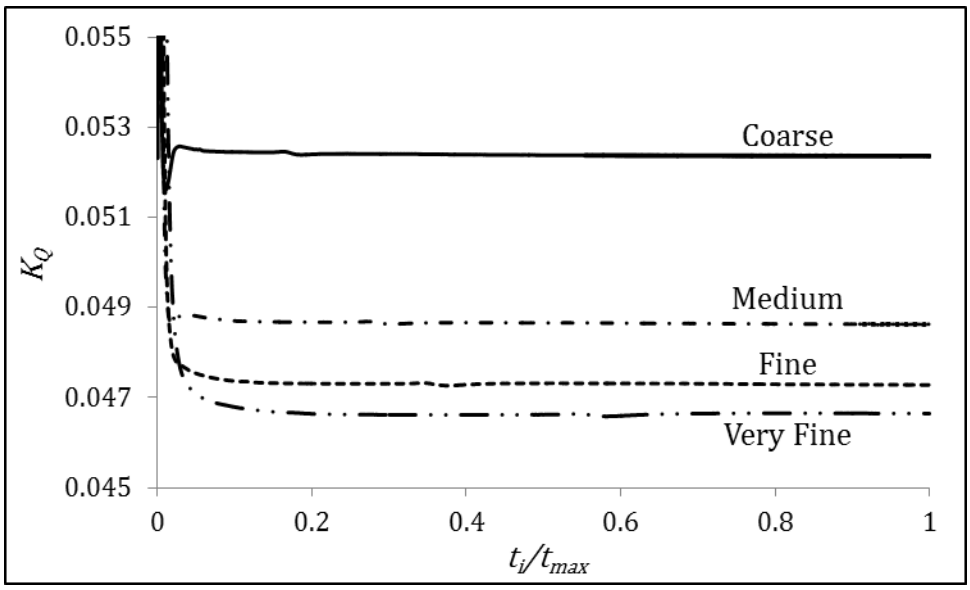

Figure 4.4: Convergence history of the torque coefficient for different grids.

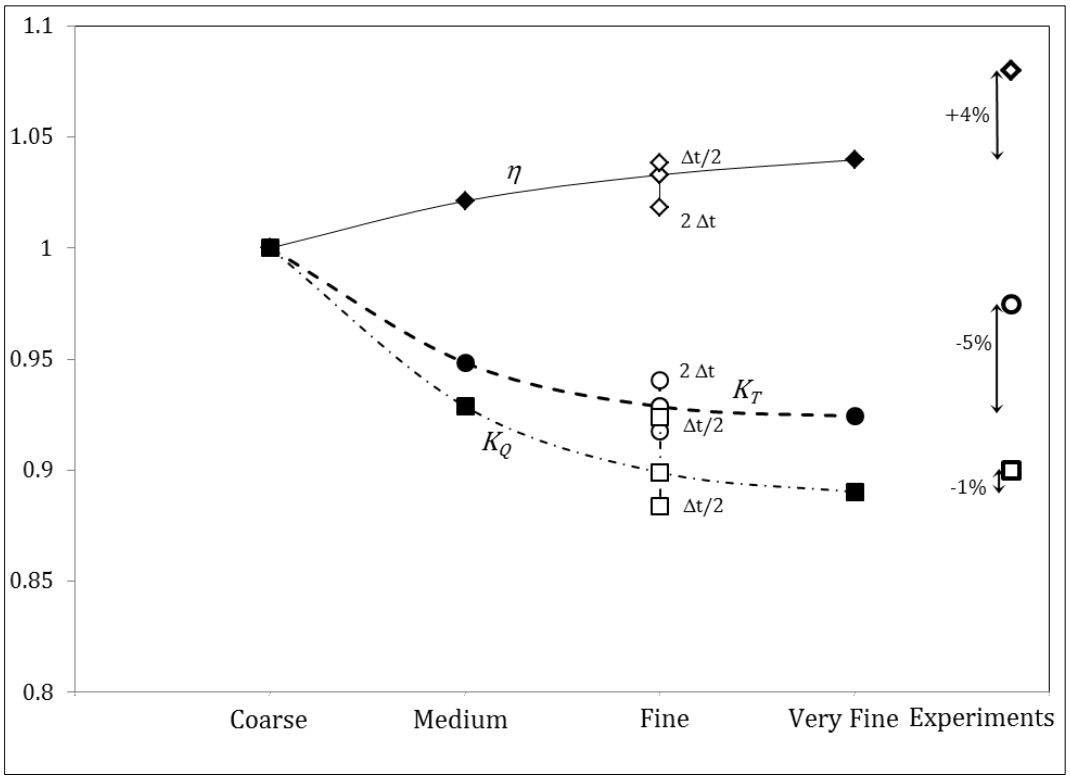

Figure 4.5: Grid and time step convergence.

The grid and time step convergence results are shown in Fig. 4.5 with K_T, K_Q, and η being nondimensionalized as $K_T/K_{T_{Coarse}}$, $K_Q/K_{Q_{Coarse}}$, and η/η_{Coarse}, respectively. Three different time steps were used for the fine grid: fine ($2\Delta t$), medium (Δt), and coarse ($\Delta t/2$) where $\Delta t = 0.00018$ (240 time steps per propeller revolution). The very fine grid simulations under predict the torque and thrust by 1% and 5% respectively, resulting in an overprediction of the efficiency of 4%. While these errors respect to the experimental values are small and consistent with other CFD for propellers, the reasons for the discrepancies are unknown.

The uncertainty analysis was done using the procedures described in (Stern et al. 2001a, 2001b) to estimate the grid and time step errors for K_T, K_Q, and η. The iterative convergence error was neglected as every time step was reasonably converged for all the variables. Table 4.4 shows the grid size and time step uncertainties for the three variables and the two groups of three grids. The overall numerical uncertainty was estimated using the group containing the very fine grid.

Table 4.4: Numerical uncertainty from grid and time step convergence for $J = 0.71$

	K_T	$10\,K_Q$	η
Grid Uncertainty (Coarse, Medium, and Fine grids)	± 0.0033	± 0.0111	± 0.0086
Grid Uncertainty (Medium, Fine, and Very Fine grids)	± 0.0004	± 0.0019	± 0.0053
Time Step Uncertainty	± 0.0450	± 0.0128	± 0.0017
CFD Result and Overall Numerical Uncertainty	0.251± 0.045	0.465± 0.017	0.611± 0.009

4.3. Open Water Curve

The OWC was created by simulating the fine propeller grid at six different advance coefficients and the wake grid at seven different coefficients. Comparison with the experimental results is shown in Fig. 4.6, where the lines show the experimental

results. The numerical results for both grids are in excellent agreement with the data, but slightly under predict thrust and torque at high propeller loads (low J) and overpredict at lower loads (high J). Besides possible limitations with the computational method, these differences between CFD and experiments could be caused by a variety of factors, among them errors arising from differences in the geometry or the presence of the driving mechanism for the shaft in the towing tank, which was neglected in the CFD computations.

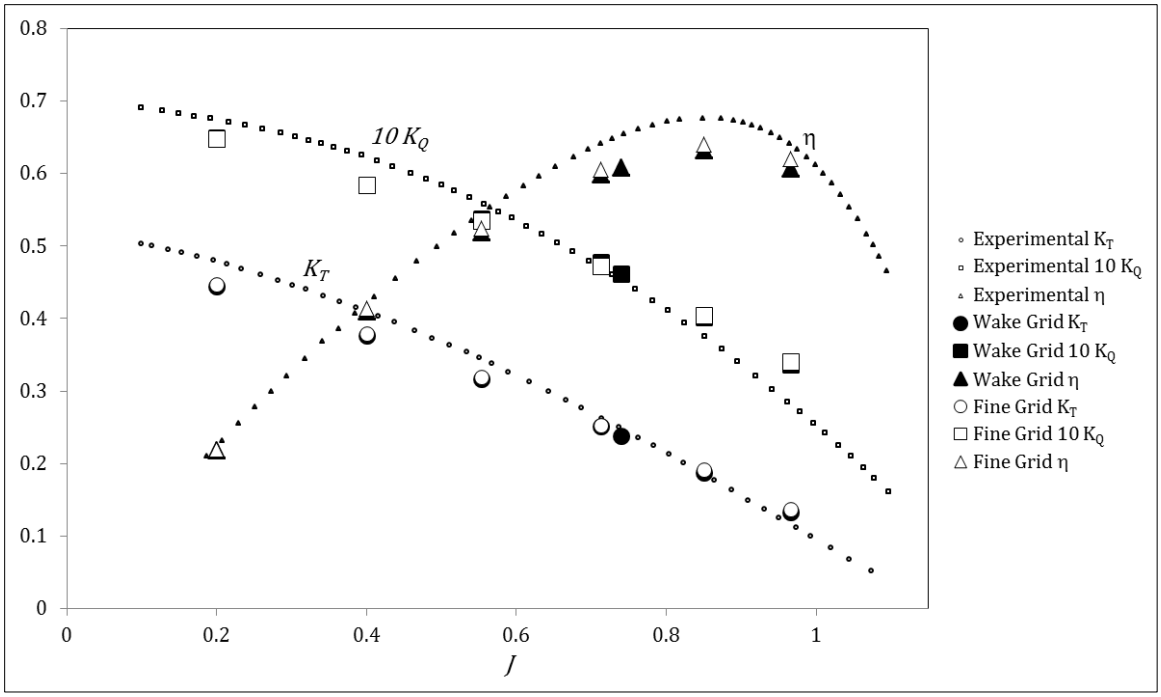

Figure 4.6: E1619 OWC for wake and fine grids.

The magnitude of the differences shown in Fig. 4.6 between CFD and experiments are consistent with other computations of open water curves for surface ship propellers (Rhee and Joshi 2005, Castro *et al.* 2011) and submarine propellers (Di Felice *et al*. 2009). This paper computed a wide range of loads ($0.2 < J < 0.96$), while Di Felice *et al.* (2009) limit their analysis to $0.74 < J < 0.85$.

4.4. Wake Analysis

4.4.1 Grid Comparison

The effects of the grid refinement on the wake are shown in Fig. 4.7, which displays isosurfaces of the second invariant of the rate of strain tensor at $Q = 12{,}000$ for the four grids. Axial velocity is indicated by levels of grey. Tip vortex pairing can be observed for the fine and very fine grids but is not resolved by the coarser grids as the lack of refinement causes the vortices to dissipate before pairing can occur. The effect of the grid refinement on the wake solution is much stronger than in the resulting forces and moments, as seen in the previous section. The strong hub vortex is visible in all levels of refinement with the details less pronounced in coarser grids.

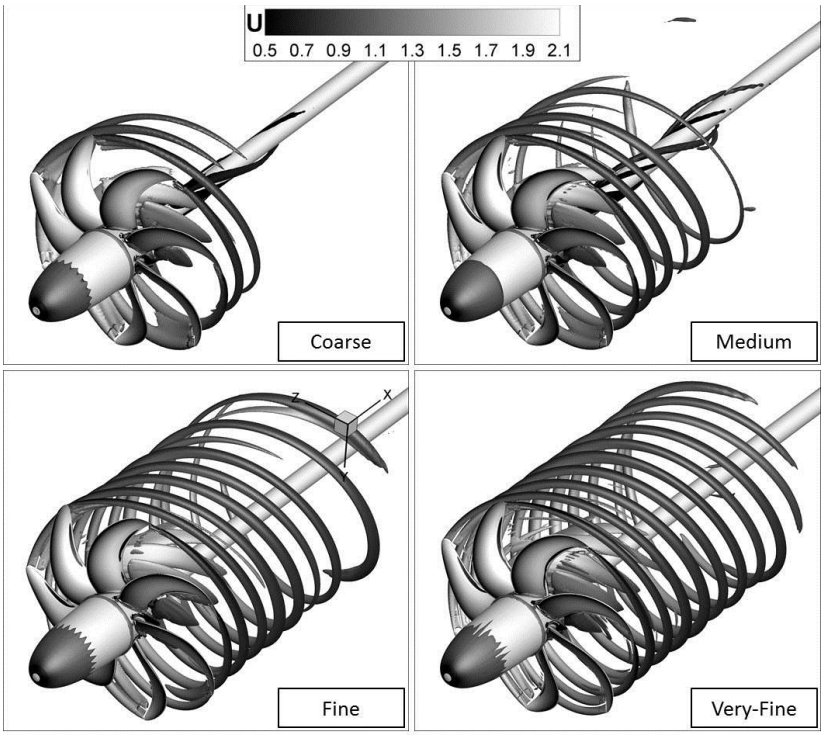

Figure 4.7: $Q = 12{,}000$ isosurfaces at $J = 0.71$ for grids using DDES.

The total vorticity at the plane $y = 0$ is shown in Fig. 4.8. Though the general vorticity patterns are similar for all grids, diffusion and loss of vorticity are dramatic for the coarser grids. Vortex pairing is evident in the fine and very fine grids as the co-rotating tip vortices merge downstream of the propeller. This phenomenon was first reported by Felli *et al*. (2011), and is more likely occur with tip vortices closer to each other. The tip vortices are closer to each other at higher loads (low J) and for propellers with more blades.

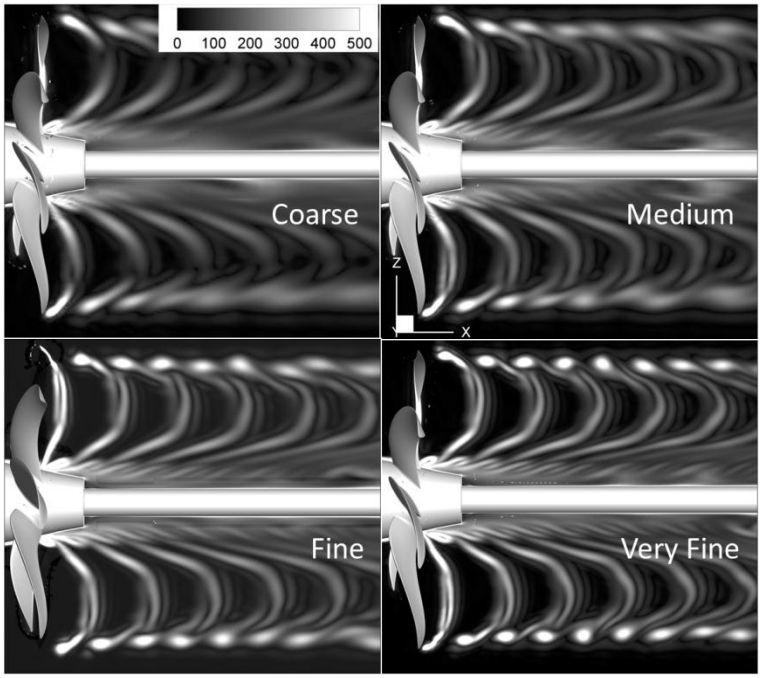

Figure 4.8: Vorticity for all grids at $J = 0.71$ using DDES.

4.4.2 Wake Grid

At this point the computations are performed using the wake grid, which provides a finer refinement in the wake region and thus suffers less from numerical diffusion than the very fine grid. One high-load advance coefficient ($J = 0.4$) that presents significant tip vortex interaction and was therefore computed with three turbulence approaches

(RANS, DES, DDES) and with no turbulence model to evaluate the effect of the resolved/unresolved turbulence on the wake and the vortex pairing process.

Vortical structures for the four different solutions are shown in Fig. 4.9, displayed as isosurfaces of $Q = 100{,}000$ greyscaled with axial velocity. For all cases the vortical structures are observed until the end of the refinement grid, where the mesh resolution becomes too coarse and the vortices are lost to diffusion.

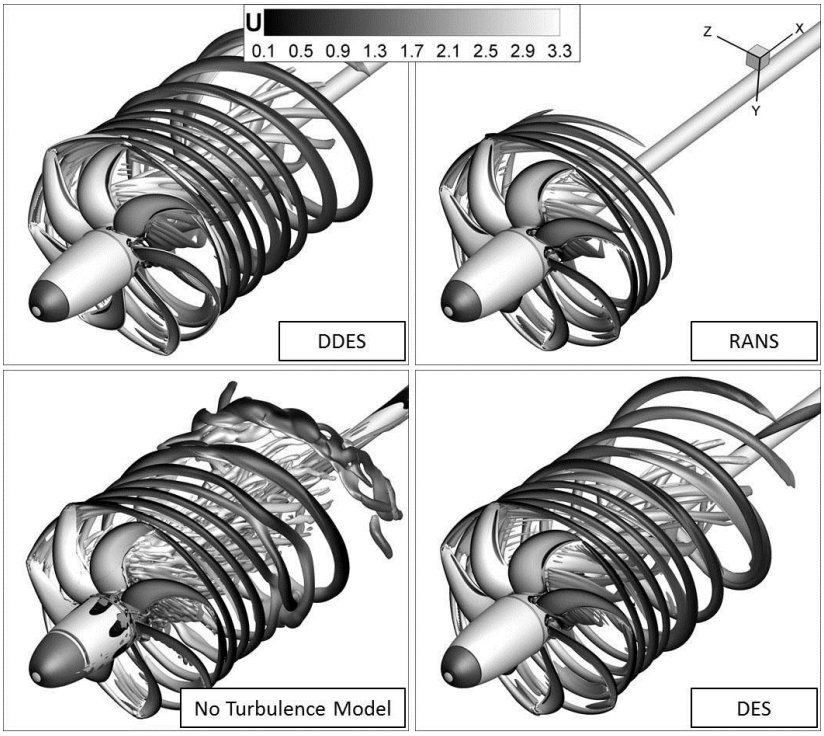

Figure 4.9: $Q = 100{,}000$ isosurfaces for different turbulence models at $J = 0.4$.

Figure 4.10 shows the total vorticity at cross sections at the plane $y = 0$ for the four solution approaches. The with no turbulence model solution has only molecular viscosity and is only subject to the small numerical diffusivity caused by the fourth-order biased scheme (Ismail et al. 2010). As expected, the RANS solution overly dissipates the tip vortices through an excess of modeled turbulent viscosity. The DES approach solves the RANS problem of excessive diffusion by transitioning from RANS to LES in well

resolved grid regions, but usually tends to over-predict separation (Spalart 2009). This problem is solved in many cases by DDES (Spalart 2009). Notice in Fig. 4.9 that the solution with no turbulence model tends to show early instability of the tip vortices and much more intense vorticity near the hub where necklace and trailing edge vortices are strong. The DES and DDES solutions are similar, though DES predicts slightly stronger vortices and thus a bit earlier pairing. The DDES solutions look more consistent with the observations of tip vortices and pairing by Felli et al. (2011), and thus the method is chosen for the following discussions.

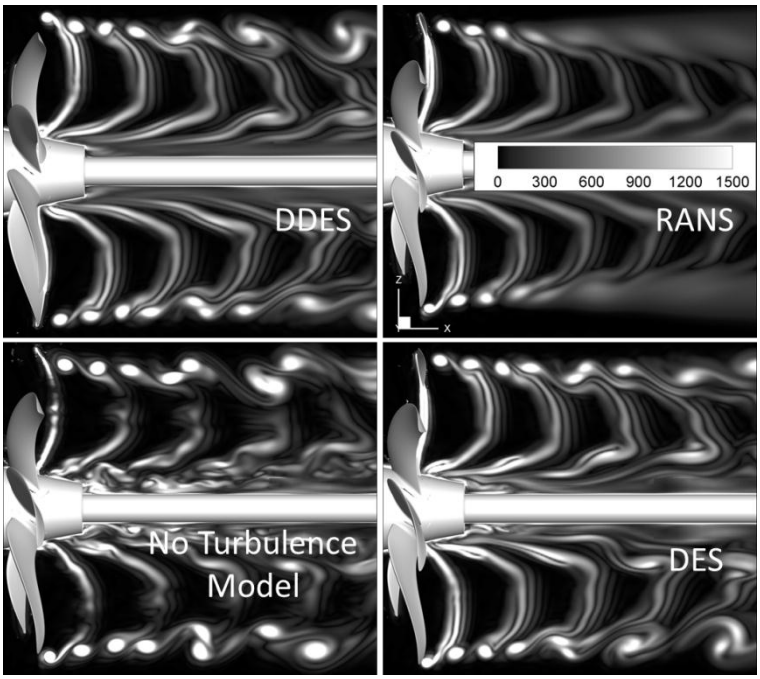

Figure 4.10: Vorticity for different turbulence models at $J = 0.4$.

The efficiency along with the torque and thrust coefficients were calculated for each method and the resulting values compared to the measured experimental values in Table 4.5. As shown in Fig. 4.6 and Table 4.5, both thrust and torque are under-predicted with CFD by about 7.8% and 5.9%, respectively, but the efficiency shows much smaller

error. The computations with no turbulence model yielded the results closest to the experimental values with a difference in efficiency of 0.63%, while the RANS solution was the least accurate with a difference in efficiency of 2.29%. DDES (1.74%) proved to be slightly more accurate than DES (1.81%), although the variance was very small.

Table 4.5: Different solver methods at $J = 0.4$

	K_T	$10\,K_Q$	η
Experimental	0.4095	0.6226	0.4175
DDES	0.3777	0.5861	0.4103
RANS	0.3740	0.5835	0.4080
No turbulence model	0.3821	0.5863	0.4149
DES	0.3772	0.5857	0.4100

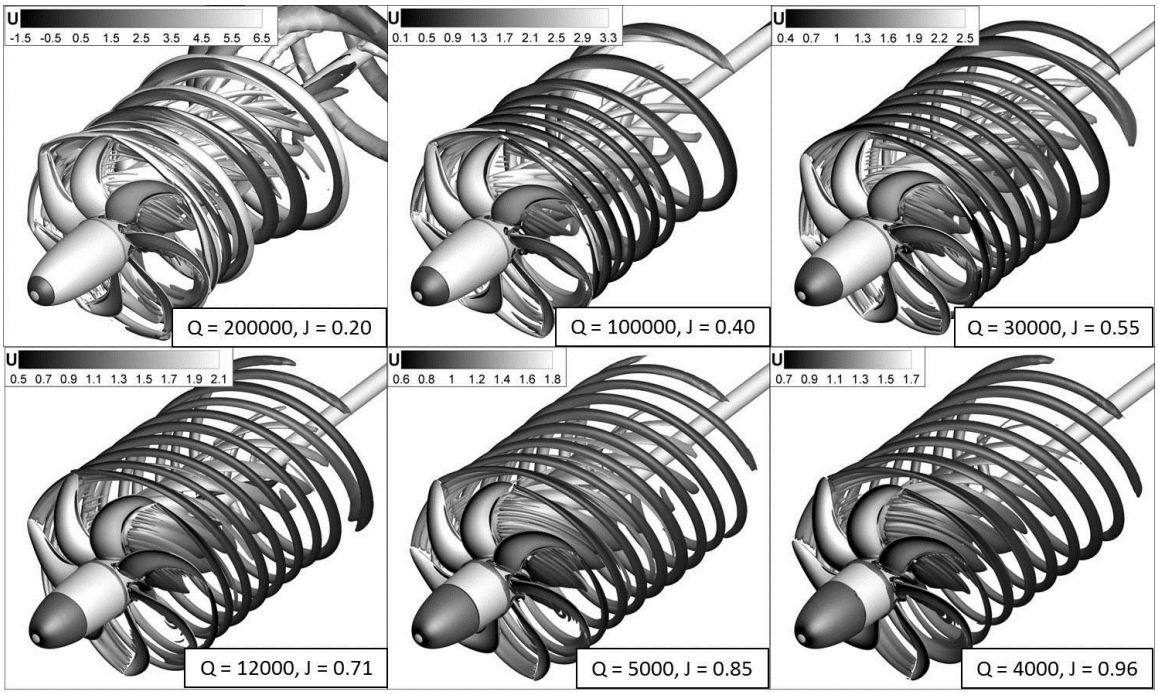

Figure 4.11: Q isosurfaces for all Js using DDES with the wake grid.

Isosurfaces of Q greyscaled with axial velocity for the six different advance coefficients computed are shown in Fig. 4.11. The Q value and axial velocity range were

altered at each J value to match the corresponding propeller induced velocity, much higher at lower J's. Vortex pairing can be observed for all J's lower than $J = 0.85$ and is delayed further downstream as the advance coefficient increases. As expected, the CFD simulations correctly predict that the strength of the tip vortices decreases as the load decreases.

Vorticity slices were taken for the six advance coefficients using the method previously described and are shown in Fig. 4.12. At higher loads it is shown that the tip vortices merge very quickly, initially in pairs of contiguous vortices, which results first in three merged pairs and a free tip vortex, then these vortices merge in pairs forming two stronger vortices, and ultimately these two also merge forming one large vortex at $J = 0.2$.

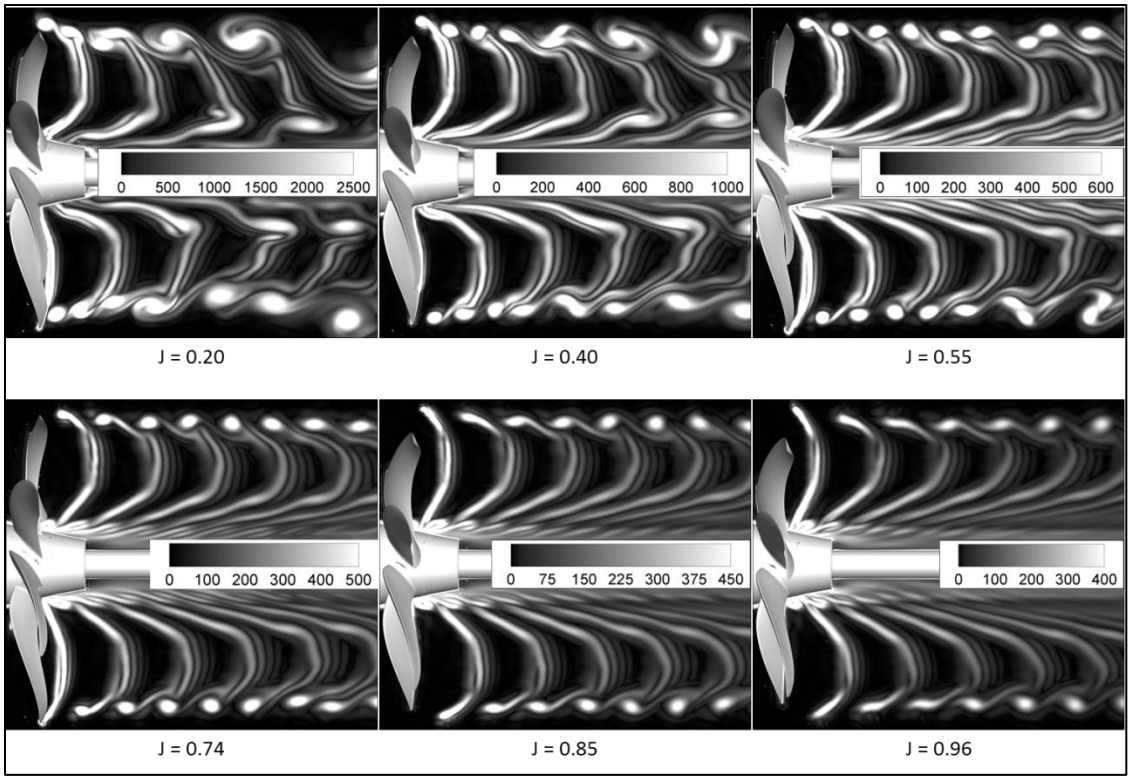

Figure 4.12: Vorticity at different J's using DDES with the wake grid.

The phenomenon of helical vortex instability was numerically studied for wind turbine rotors by Ivanell *et al*. (2010), who found pairing occurred several rotor radii downstream of the hub for their conditions. Felli *et al*. (2011) observed that closer tip vortices resulted in faster induction pairing. To reduce the distance between vortices and study pairing the authors used higher advance coefficient for the same propeller geometry or larger number of blades for the same advance coefficient. These two mechanisms in a marine propeller lead to larger induced wake velocities and thus larger contraction of the wake, favoring stronger mutual vortex induction and pairing over expanding wakes as is the case of a wind turbine rotor.

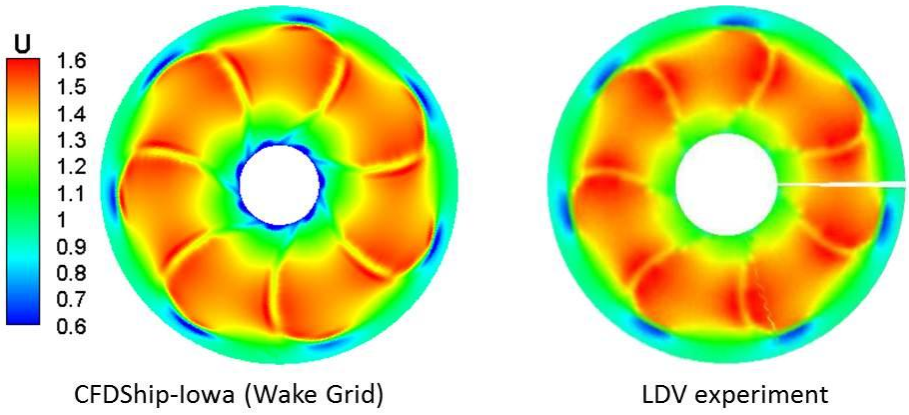

Figure 4.13: Propeller velocity for $J = 0.74$ at $x = 0.17\ R$ (data from Liefvendahl *et al.* 2010).

Figure 4.13 shows computed and experimental normalized axial velocity at $x = 0.17\ R$ downstream of the propeller plane for $J = 0.74$, where R is the radius of the propeller. The computations were performed with DDES on the wake grid, while the experimental results were reported by Liefvendahl *et al*. (2010). The similarities between CFD and experiments are remarkable, including the maximum velocity in the wake of the

blades, the velocity deficit induced by the tip vortices, and the acceleration around the low velocity region in the trailing edge of the blades.

CHAPTER 5

SELF-PROPULSION

5.1. Simulation Conditions

Table 5.1: DARPA Suboff self-propelled by INSEAN E1619 main parameters

Reynolds number	1.2×10^7
	DARPA Suboff
Hull Diameter [m]	0.508
Hull Length [m]	4.356
	INSEAN E1619
Propeller diameter [m]	0.262

A simulation of the DARPA Suboff fitted with the E1619 propeller under self-propelled conditions was performed using DDES and the methodology described in Carrica *et al*. (2010). Geometric details are similar to those used by Liefvendahl *et al*. (2010), and are shown in Table 5.1. The grid is composed of overset blocks to build the hull, sail, rudders, stern planes, and propeller. The assembly of individual meshes is highlighted in Fig. 5.1, using different colors to denote each grid.

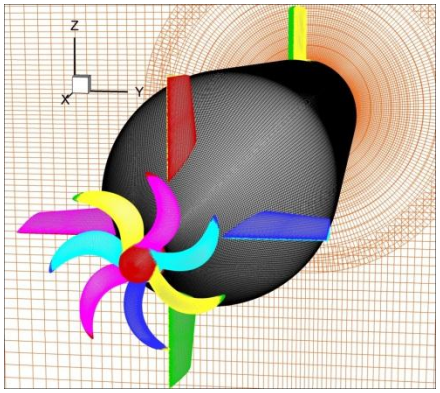

Figure 5.1: Grid for self-propelled submarine computations.

Table 5.2: Grid dimensions for self-propelled grid

Grid	Size	Total Points	Type
Hull	481x101x241	11.7 M	‘O‘
Nose	61x51x61	190 k	Wrapped
Sail	2x61x51x121	2x376 k	Wrapped
Rudders	4x61x51x121	4x376 k	Wrapped
Stern Planes	4x61x51x121	4x376 k	Wrapped
Propeller Hub	101x37x101	377 k	‘O’
Blades	7x101x37x101	7x377 k	‘O’
Tips	7x61x51x61	7x190 k	Wrapped
Refinement Gaps for Appendages	4x84x87x26	4x190 k	Curvilinear Block
Refinement Wake	241x221x221	11.8 M	Cartesian
Refinement Wake	119x79x79	743 k	Cartesian
Background	187x109x109	2.22 M	Cartesian
Total		38.5 M	

The grid dimensions for the self-propelled submarine are shown in Table 5.2. The blade and tip grids around the propeller are the same as the medium grid from the grid study. The grids that make up the propeller rotate as a child of the submarine. The submarine and all related grids can move forward in surge, resulting in a computation in an Earth-fixed inertial coordinate system. The computations for the self-propulsion case use the same time step and reference values for length and velocity as the propeller open-water curve case. A PI controller as described in Eq. (17) was used to modify the rotational speed of the propeller, and to speed up the computation the inertia of the submarine was reduced by a factor of 10, resulting in faster acceleration but in the same steady-state self-propulsion result. Convergence of the propeller rotational speed and boat speed during the self-propulsion computation is shown in Fig. 5.2.

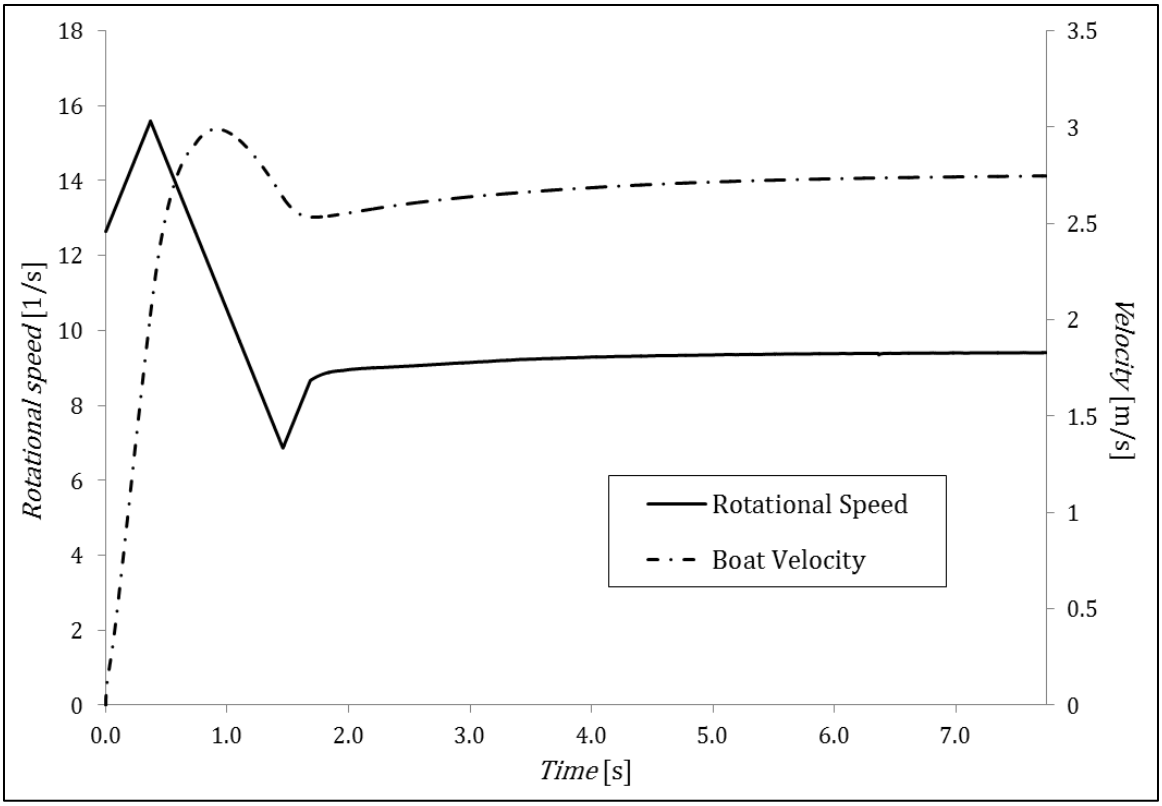

Figure 5.2: Convergence history of boat velocity and propeller rotational speed.

5.2. Self-propelled Analysis

The thrust and torque coefficients were obtained by direct integration of the pressure and viscous forces on the propeller blades, and are shown in Table 5.3. To obtain the advance coefficient at self-propulsion the thrust identity method was used, in which the thrust coefficient is entered in the OWC and the corresponding advance coefficient is obtained. The numerical or the experimental OWC can be used, but using the OWC computed with CFD results in a fully predictive methodology (Castro *et al.* 2011). Table 5.3 shows the results obtained with both approaches. Using the numerical OWC the predicted advance coefficient is $J = 0.7498$, 2.1% lower than the advance coefficient predicted with the experimental OWC. The corresponding advance velocities are $V_a = 0.6707$ and $V_a = 0.6851$ for the CFD OWC and EFD OWC, respectively. The propeller efficiency behind the hull is $\eta = 0.5927$, 3.1% smaller than the obtained from

the OWC at the same operating point. These results are very close to those reported by Liefvendahl and Tröeng (2011) for their computations of Suboff using a LES method.

Table 5.3: Self-propelled solution at $U = 2.75$ m/s

	K_T	$10\,K_Q$ (CFD or OWC)	η (CFD or OWC)	J	V_a
Self-Propelled	0.2342	0.4714	0.5927	-	-
Using CFD OWC	0.2342	0.4577	0.6115	0.7498	0.6707
Using Experimental OWC	0.2342	0.4353	0.6602	0.7659	0.6851

Cross-sectional cuts showing the instantaneous axial velocity at two different axial planes behind the propeller can be found in Fig. 5.3, along with a cross section at the plane $y = 0$. The far-field velocity for this computation is $U_0 = 0$, since the simulation is performed in an Earth-fixed coordinate system. The slice at $x/L = 0.975$ is comparable to the slice shown in Fig. 4.13. Notice the effect of the wake of the submarine, which results in lower velocity behind the propeller closer to the hub, and consequently higher load. At approximately 40 degrees from the top the wake of the sail can be observed as a low velocity section and a stronger tip vortex due to the increased load and leakage. At $x/L = 1.04$ the effect of the sail is more noticeable and the induced rotation inside the propeller wake has caused a significant distortion of the original flow field. The decreasing radius of the wake as the flow accelerates behind the propeller is evident, induced by both the propeller and the convergence of the flow behind the hull.

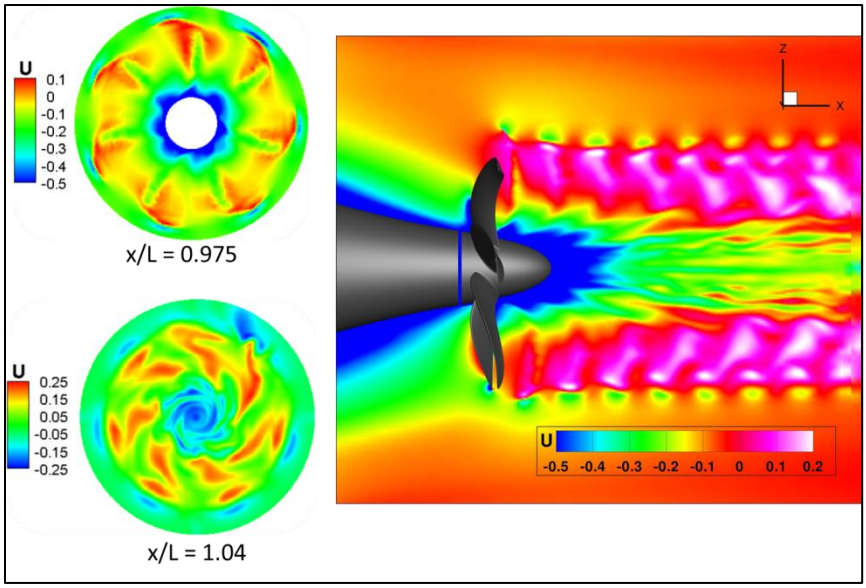

Figure 5.3: Cross sections of the wake at two axial positions (left) and at $y = 0$ (right) for self-propelled submarine.

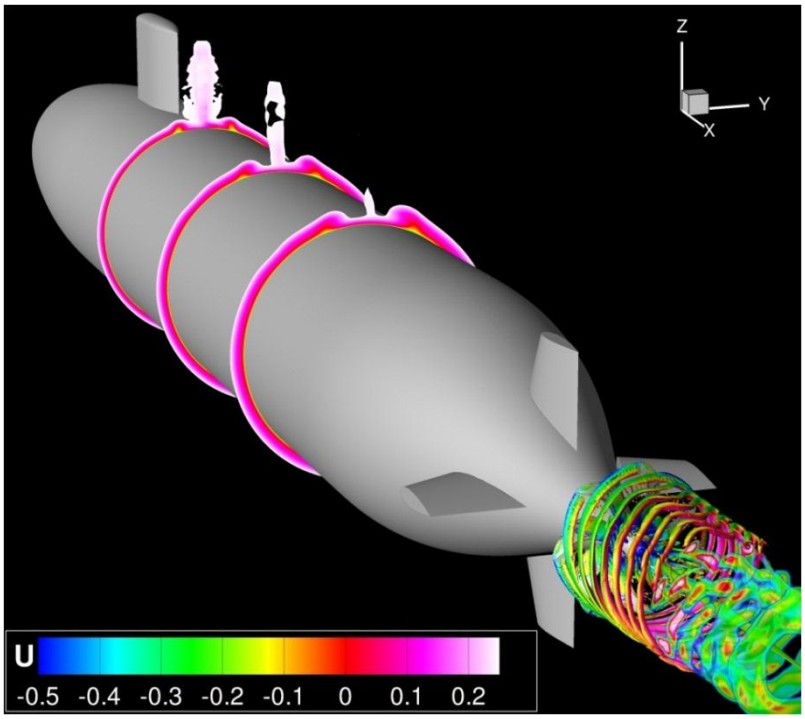

Figure 5.4: View of the self-propelled DARPA Suboff submarine with vortical structures as isosurfaces of $Q = 10000$.

Figure 5.4 shows a view of the instantaneous solution of the submarine in self-propelled condition. The propeller tip vortices are shown as isosurfaces of $Q = 10000$ colored with axial velocity, and cross-sectional also colored with axial velocity show the wake of the sail and propeller. The effect of the wake of the submarine appendages in the propeller tip vortices is evident, with a significant deviation from a symmetric helicoid mainly in the wake of the sail. The solution loses the tip vortices to diffusion when the refinement grid ends downstream of the propeller.

5.3. Blade Analysis

While the wake of the boat significantly affects the performance of the propeller, it also produces substantial instantaneous loads in each blade. Figure 5.5 shows the thrust coefficient of blades 1, 2 and 7, three adjacent blades.

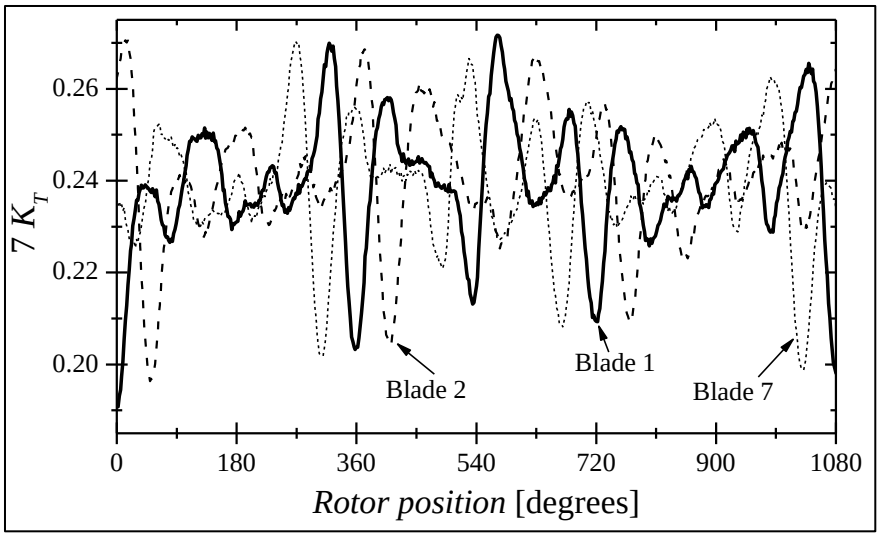

Figure 5.5: Thrust coefficient of three contiguous blades for three full rotations of the propeller. Blade 1 is on top at 0 degrees, with blade 2 the next one to port and blade 7 the previous to starboard.

Blade 1 is on top at 0 degree rotation of the propeller, while blades 2 and 7 are 51.43 degrees to port and starboard, respectively. Notice in Fig. 5.5 that the peak to peak fluctuations in thrust reach about 34% of the average thrust coefficient. The minimum thrust occurs when the blades go through the top crossing the wake of the sail and the maximum immediately before, which occurs approximately 40 degrees to port in this right-handed propeller (angle in Fig. 5.5 increases clockwise looking at the propeller from the stern).

The minimum thrust is due to the wake of the high speed downstream of the sail caused by the boundary layer thinning resulting from the action of the necklace vortex created by the sail, see Fig. 5.4. The wake in an axial plane $R/2$ upstream of the propeller, presented in Fig. 5.6, shows the high axial speed region on top, and also the low axial speed wake around it caused by the same necklace vortices. In these low speed regions the load on the blades increases due to a locally lower advance velocity and resulting higher effective angle of attack. Figure 5.6 also shows significant fluctuations around this general behavior for different revolutions, though less energetic than those predicted by Liefvendahl and Tröeng (2011) with their LES computations. The wake of the rudders and stern planes are clearly visible, though relatively weak. Strong unsteady vortices are present at about 120 and 160 degrees, and cause unsteady peaks in blade thrust. These vortices are also necklace type and originated in the root of the rudders and stern planes.

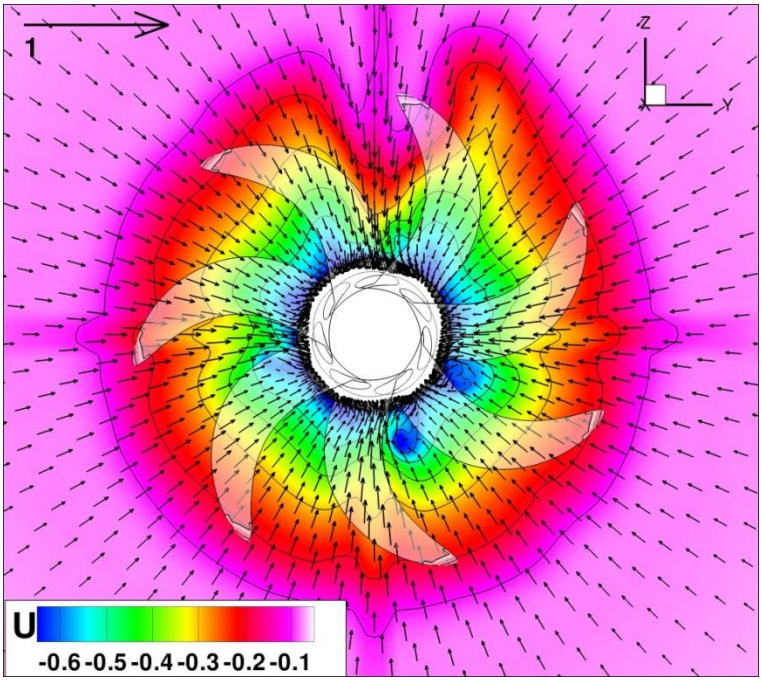

Figure 5.6: Instantaneous wake at an axial location $R/2$ upstream of the propeller. Every 11^{th} vector is shown for clarity.

CHAPTER 6

CONCLUSIONS AND RECOMMENDATIONS FOR FUTURE WORK

6.1. Conclusions

Results of a CFD study of the DARPA Suboff generic submarine hull fitted with sail, rudders, stern planes, and submarine propeller E1619 have been presented. The CFD computations were performed with a Delayed Detached Eddy Simulation approach. The CFD wake of the submarine was in good agreement with the experimental data but tended to overpredict the turbulence caused by the appendages. A rotating arm simulation of the boat showed large disturbances of the wake caused by the necklace wake generated at the sail that could result in large load fluctuations on the propeller blades.

The predicted propeller open water curves for the generic propeller E1619 are close to the experimental data, but tend to underpredict thrust and torque at high loads and overpredict for lower loads. The verification study, performed on four grids and three time steps for $J = 0.71$, shows that the thrust, torque and efficiency converge faster in grid than in time step, and also that the wake is much more affected by the grid refinement than the forces and moments. The wake of the propeller was analyzed with a grid specifically refined to capture the tip vortices. A study of different turbulence models at $J = 0.4$ shows that RANS overly dissipates the wake and that in the solution with no turbulence model the tip vortices quickly become physically unstable. DES and DDES provide similar results, with DES showing slightly more vortex mutual induction. Tip vortex pairing, studied experimentally by Felli *et al.* (2011) was observed at high loads, showing multiple vortices merging for $J \leq 0.4$. The agreement of CFD with experiments on the near wake axial velocities for $J = 0.74$ is excellent.

Self-propulsion computations of the DARPA Suboff generic submarine hull fitted with sail, rudders, stern planes and the E1619 propeller were performed in model scale and the resulting propeller performance analyzed for conditions similar to those used by

Liefvendahl *et al.* (2010). The thrust identity method was used to obtain an effective advance coefficient and advance velocity, and to compare the operating efficiency with the open water efficiency. The results show that the same methodology applied to surface ships by Carrica *et al*. (2010) and Castro *et al*. (2011) can be used to compute self-propulsion of submarines.

6.2. Recommendations for Future Work

Future work is focused on coupling CFDShip-Iowa V4.5 with the potential flow propeller solver PUF-14, with the goal of realizing substantial time savings over discretized propeller computations, while still accounting for inhomogeneous and transient wakes. The coupled solver needs to be validated for the E1619 propeller using the experimental results previously described. After validation, CFDShip/PUF could be used with the Suboff submarine to estimate self-propulsion and compare with the discretized propeller for different maneuvers. The coupled solver could also be used to evaluate other submarines under self-propulsion.

REFERENCES

Alin N., Bensow R.E., Fureby C., Huuva T., and Svennberge U. 2010. "Current Capabilities of DES and LES for Submarines at Straight Course," *J. Ship Research* 54, pp. 184-196.

Atsavapranee P. 2010. "Experimental Measurements for CFD Validation of the Flow about a Submarine Model (Suboff)," *Submarine Hydrodyn. Working Group Meeting*, Bethesda, MD, USA.

Boger DA, Dreyer JJ. 2006. Prediction of hydrodynamic forces and moments for underwater vehicles using overset grids. *AIAA Paper 2006-1148*, 44th AIAA Aerospace Sciences Meeting, Reno, NV, USA.

Bull, P. 1996. "The validation of CFD predictions of nominal wake for the SUBOFF fully appended geometry," Twenty-first Symposium on Naval Hydrodynamics. Trondheim, Norway.

Califano A, Steen S. 2011. Numerical simulations of a fully submerged propeller subject to ventilation. *Ocean Eng*. **38**, 1582-1599.

Carrica PM, Wilson RV, Stern F. 2007a. An unsteady single-phase level set method for viscous free surface flows. *Int. J. Numer. Meth. Fluids* **53**, 229-256.

Carrica PM, Wilson RV, Noack RW, Stern F. 2007b. Ship motions using single-phase level set with dynamic overset grids *Comput. Fluids* **36**, 1415-1433.

Carrica PM, Castro AM, Stern F. 2010. Self-propulsion computations using a speed controller and a discretized propeller with dynamic overset grids. *J. Mar. Sci. Technol.* **15**, 316-330.

Carrica PM, Fu H, Stern F. 2011. Computation of self-propulsion free to sink and trim and of motions in head waves of the KRISO Container Ship (KCS) model. *Appl. Ocean Res.* **33**, 309-320.

Castro AM, Carrica PM, Stern F. 2011. Full scale self-propulsion computations using discretized propeller for the KRISO container ship KCS. *Comput. Fluids* **51**, 35-47.

Crook B. 1990. Resistance for DARPA Suboff as Represented by Model 5470. David Taylor Research Center report DTRC/SHD-1298-07.

Denny S. 1968. Cavitation and open-water performance tests of a series of propellers designed by lifting-surface methods. Naval Ship Research and Development Center report 2878, Naval Ship Research and Development Center, Department of the Navy.

Di Felice F, Felli M, Liefvendahl M, Svennberg U. 2009. Numerical and experimental analysis of the wake behavior of a generic submarine propeller. *First Int. Symp. Marine Propulsors*, Trondheim, Norway.

Felli M, Guj G, Camussi R. 2008. Effect of the number of blades on propeller wake evolution. *Exp. Fluids* **44**, 409-418.

Felli M, Camussi R, Di Felice F. 2011. Mechanisms of evolution of the propeller wake in the transition and far fields. *J. Fluid Mech.* **150**, 1-49.

Fuhs, D. 2005. Evaluation of Propeller Unsteady Force Codes for Noncavitating Conditions. *NSWCCD-50-TR-2005/004*. Naval Surface Warfare Center - Carderock Division, Department of the Navy.

Gatchell S, Hafermann D, Streckwall H. 2011. Open Water Test Propeller Performance and Cavitation Behaviour using PPB and FreSCo. *Second Int. Symp. Marine Propulsors*, Hamburg, Germany.

Groves N, Huang T, Chang M. 1989. Geometric characteristics of DARPA Suboff models. *DTRC/SHD-1298-01*. David Taylor Research Center – Ship Hydromechanics Department, Department of the Navy.

Hsiao C, Pauley L. 1999. Numerical Computation of Tip Vortex Flow Generated by a Marine Propeller. *J. Fluid Eng*. **121**, 638-645. Inoue M, Kuroumaru M (1984) Three-dimensional structure and decay of vortices behind an axial flow rotating blade row. *J. Eng. Gas Turbines Power* **106**, 561-569.

Inoue M, Kuroumaru M. 1984. Three-dimensional structure and decay of vortices behind an axial flow rotating blade row. *J. Eng. Gas Turbines Power* **106**, 561-569.

International Towing Tank Conference. 2002. Propulsion, Propulsor, Uncertainty Analysis, Example for Open Water Test. ITTC – Recommended Procedures.

Ismail F, Carrica PM, Xing T, Stern F. 2010. Evaluation of Linear and Non-Linear Convection Schemes on Multidimensional Non-Orthogonal Grids with Applications to KVLCC2 Tanker. *Int. J. Num. Meth. Fluids* **64**, 850-886.

Ivanell S, Mikkelsen R, Sørensen JN, Henningson D. 2010. Stability analysis of the tip vortices of a wind turbine. *Wind Energy* **13**, 705–715.

Liefvendahl M, Alin N, Chapuis M, Fureby C, Svennberg U, Tröeng C. 2010. Ship and propulsor hydrodynamics. *V European Conference on Comput. Fluid Dynamics*, Lisbon, Portugal

Liefvendahl M, Tröeng C. 2011. Computation of cycle-to-cycle variation in blade load for a submarine propeller using LES. *Second Int. Symp. Marine Propulsors*, Hamburg, Germany.

Menter FR. 1994. 2-equation Eddy Viscosity Turbulence Models per Engineering Applications. *AIAA J.* **32**, 1598-1605.

Noack R. 2005. Suggar: a general capability for moving body overset grid assembly. *AIAA paper 2005-5117*, 17th AIAA Computational Fluid Dynamics Conf., Toronto, ON, Canada.

Rhee S, Joshi S. 2005. Computational Validation for Flow around a Marine Propeller Using Unstructed Mesh Based Navier-Stokes Solver. *JSME Int. J.* **48**, 562-570

Stern F, Wilson R, Coleman H, Paterson E. 2001a. Comprehensive approach to verification and validation of CFD simulations—Part 1: Methodology and procedures. *J. Fluids Eng.* **123**, 793-802

Stern F, Wilson R, Coleman H, Paterson E. 2001b. Comprehensive approach to verification and validation of CFD simulations—Part 2: Application for RANS simulation of a cargo/container ship. *J. Fluids Eng.* **123**, 803-810

Spalart P. 2009. Detached Eddy Simulation. *Annu. Rev. Fluid Mech.* **41**, 181–202

Watanabe T, Kawamura T, Takekoshi Y, Maeda M, Rhee S. 2003. Simulation of steady and unsteady cavitation on a marine propeller using a RANS CFD code. *Fifth Int. Symp. Cavitation*, Osaka, Japan.

Xing T, Kandasamy M, Stern F. 2007. Unsteady free-surface wave-induced separation: analysis of turbulent structures using detached eddy simulation and single-phase level set. *J. Turbulence* **8**, 1-35

Xing T, Carrica PM, Stern F. 2010. Large-scale RANS and DDES computations of KVLCC2 at drift angle 0 degree. A Workshop on Numerical Ship Hydrodynamics, Gothenburg, Sweden

Young Y, Kinnas S. 2003. Analysis of supercavitating and surface-piercing propeller flows via BEM. *Comput. Mech.* **32**, 269-280.

Yu-cun P, Huai-xin Z. 2010. Numerical Hydro-Acoustic Prediction of Marine Propeller Noise. *J. Shanghai Jiaotong Univ. (Sci.)* **15**, 707-712.